International Journal of Solids and Structures 292 (2024) 112724

Contents lists available at ScienceDirect

International Journal of Solids and Structures

journal homepage: www.elsevier.com/locate/ijsolstr

Exploring novel mechanical metamaterials: Unravelling deformation mode coupling and size effects through second-order computational homogenisation

Wanderson F. dos Santos [a,b], Igor A. Rodrigues Lopes [c,b], Francisco M. Andrade Pires [c,*], Sergio P.B. Proença [a]

[a] Departamento de Engenharia de Estruturas, Escola de Engenharia de São Carlos, Universidade de São Paulo, Av. Trabalhador São-Carlense, 13566-590 São Carlos, Brazil
[b] DEMec, Faculdade de Engenharia, Universidade do Porto, Rua Dr. Roberto Frias, 4200-465 Porto, Portugal
[c] INEGI, Instituto de Ciência e Inovação em Engenharia Mecânica e Engenharia Industrial, Rua Dr. Roberto Frias, 400, 4200-465 Porto, Portugal

ARTICLE INFO

Keywords:
Multi-scale modelling
Finite strains
Architected materials
Coupling deformation mechanisms
Size effects

ABSTRACT

Architected materials and mechanical metamaterials are known for their unique macroscopic properties and complex behaviour that often defy conventional continuum mechanics. Therefore, in this contribution, a recent multi-scale second-order computational homogenisation method (Dos Santos et al., 2023) is employed to explore these materials under finite strains. The approach combines a second gradient continuum theory at the macro-scale and a representative volume element (RVE) with classical first-order continuum mechanics at the micro-scale. The Method of Multi-scale Virtual Power ensures a consistent scale transition. The predictive capability and applicability of the second-order computational strategy are evaluated through coupled multi-scale numerical simulations. These simulations involve two- and three-dimensional problems, with a strong focus on the development of novel metamaterials, while also accounting for diverse loading conditions, such as tension/compression-induced undulation, bending, and compression-induced torsion. Comparisons with first-order homogenisation and Direct Numerical Simulations validate the approach. Analysis of homogenised consistent tangents reveals valuable insights into macroscopic properties. Overall, the results highlight the capability of the second-order strategy to capture significant phenomena, including second-order deformation modes, coupling deformation mechanisms, and size effects.

1. Introduction

Architected materials and mechanical metamaterials play a pivotal role in various engineering domains, spanning construction, aerospace, automotive, and biomedical industries. These innovative materials are carefully engineered by exerting precise control over the geometric configuration and the mechanical properties of their constituent elements, often at the micro-scale or meso-scale. Consequently, these cutting-edge structures exhibit remarkable mechanical strength and/or unique attributes rarely encountered in natural materials. Moreover, these advanced materials pave the way for ground-breaking high-performance applications in the realm of materials science, pushing the boundaries of what can be achieved.

Within the domain of advanced engineered materials, we will focus on two distinct classes: artificially architected materials and mechanical metamaterials. The first class, encompassing cellular and lattice structures, offers a remarkable array of characteristics, including low density, large surface area, and high stiffness and strength. These architected materials find versatile utility in multifunctional applications (Pan et al., 2020; Qi et al., 2021; Benedetti et al., 2021; du Plessis et al., 2022; Yin et al., 2023), such as lightweight materials and/or high specific strength and stiffness (Schaedler et al., 2011; Meza et al., 2014; Zheng et al., 2014; Zhang et al., 2019; Kang et al., 2019), energy absorption capabilities (Chen et al., 2020; Alberdi et al., 2020; Guo et al., 2021; Song et al., 2019; Cheng et al., 2023), vibration damping (Syam et al., 2018; Rifaie et al., 2022), enhanced thermo-mechanical properties for heat dissipation (Catchpole-Smith et al., 2019; Sajjad et al., 2022), and effective acoustic energy damping or sound absorption (An et al., 2021; Li et al., 2023). In essence, cellular and lattice structures emerge as adaptable solutions to a wide array of real-world challenges (Jia et al., 2020).

* Corresponding author.
E-mail address: fpires@fe.up.pt (Francisco M. Andrade Pires).

https://doi.org/10.1016/j.ijsolstr.2024.112724
Received 1 November 2023; Received in revised form 9 February 2024; Accepted 18 February 2024
Available online 23 February 2024

On the other hand, the second class, mechanical metamaterials, presents a novel dimension of materials engineering. Mechanical metamaterials can be classified as the type or subclass of architected materials, where artificial materials are rationally designed to exhibit superior mechanical performance, unprecedented mechanical behaviours and/or outstanding properties (Jiao et al., 2023). Hence, these materials exhibiting unconventional responses introduce a new paradigm in materials science, with unique properties and behaviours, including negative Poisson's ratio (auxetic materials) (Lakes, 1987; Babaee et al., 2013; Mukhopadhyay and Adhikari, 2016; Mizzi et al., 2018; Su et al., 2022; Zhang et al., 2022), negative compressibility (Baughman et al., 1998; Gatt and Grima, 2008; Lakes et al., 2012; Nicolaou and Motter, 2012), pattern transformations (multi-stable mechanical metamaterials) (Mullin, 2007; Bertoldi et al., 2008, 2010; Gao et al., 2018; van Bree et al., 2020), ultralight and ultra-stiff characteristics (Zheng et al., 2014; Bauer et al., 2016; Li and Gao, 2016), and twisting induced by uniaxial forces under tension or compression (Frenzel et al., 2017; Fernandez-Corbaton et al., 2019; Zhong et al., 2019; Qi et al., 2020; Wang and Liu, 2020; Xu et al., 2023; Lemkalli et al., 2023). Furthermore, mechanical metamaterials are particularly intriguing for their capacity to combine lightweight construction with exceptional energy absorption, mechanical strength, and stiffness, all while maintaining low density (Rico-Baeza et al., 2023). For those seeking a deeper understanding of metamaterials, comprehensive reviews by Yu et al. (2018), Surjadi et al. (2019), and Wu et al. (2019) offer valuable insights into this exciting field.

While architected materials and mechanical metamaterials present clear advantages over conventional materials with predetermined properties, their remarkable capabilities stem from their intricate microstructures. Therefore, the modelling and design of these materials pose significant challenges due to the difficult interplay of effects observed at smaller scales. These typically include high-order effects, such as size and localisation effects, which manifest in both architected materials and mechanical metamaterials. The size dependence associated with the material microstructure or structural microarchitecture has been well-documented in numerous experiments (Hosseini and Niiranen, 2022). Significant research efforts have been devoted to exploring size effects in architected structures and metamaterials under various loading conditions, including bending (Yoder et al., 2018; Khakalo et al., 2018; Yang and Müller, 2021; Hosseini and Niiranen, 2022; Sarhil et al., 2023; Yang et al., 2021) and axial tension/compression-induced torsion (Duan et al., 2018; Khakalo et al., 2018; Zheng et al., 2019; Ziemke et al., 2019; Frenzel et al., 2021; Xu et al., 2023). As a result, more advanced theories may be necessary to address the complexities of deformation modes, including those involving negative Poisson's ratio, tension/compression-induced torsion, pattern transformations, higher strain gradients, and high curvatures, among other intricate phenomena.

Regarding the mechanical modelling for metamaterials and architected materials, it becomes evident that the classical small-strain theory, or the conventional strain-based Cauchy theory, falls short in capturing size effects. In this context, the so-called generalised continua or higher-order continuum mechanics emerges as an interesting avenue for effectively modelling high-order effects. Generalised continua theories have been employed in the study of metamaterials and architected structures (Ganghoffer et al., 2023), such as: (i) Micromorphic continuum theory (Rokoš et al., 2019; Biswas et al., 2020; Rokoš et al., 2020; van Bree et al., 2020; Sarhil et al., 2023), (ii) Cosserat or micropolar theories (Kumar and McDowell, 2004; Alavi et al., 2022; Dos Reis and Ganghoffer, 2012; Yoder et al., 2018; Duan et al., 2018; Lemkalli et al., 2023), (iii) strain gradient continua approaches (Yang et al., 2020; Yang and Müller, 2021; Yang et al., 2022; Vazic and Newell, 2023; Yang et al., 2021). Furthermore, an alternative method for modelling metamaterials and architected materials involves Direct Numerical Simulations at the macro-scale. This approach explicitly represents the internal structure's geometry on the macro-scale by employing an arrangement of unit cells. However, it is essential to note that this method can entail a high computational cost, including substantial memory requirements, especially when conducting simulations with numerous unit cells.

Multi-scale strategies that employ second-order computational homogenisation offer intriguing and versatile approaches for modelling metamaterials and architected materials, especially when considering second-order effects. This involves incorporating strain gradient elasticity, often referred to as second gradient elasticity, into the continuum description to improve the accuracy of the model. Consequently, these second-order homogenisation theories serve as compelling alternatives to the limitations associated with first-order homogenisation, which predominantly address tension/compression and shear deformation modes at the micro-scale while neglecting size effects. On the other hand, second-order homogenisation methods enable a more comprehensive treatment of second-order deformation modes, such as bending and torsion, and also account for size effects more effectively.

Over time, numerous studies focusing on second-order computational homogenisation have emerged and evolved. Pioneering work was performed by Geers et al. (2003) and Kouznetsova et al. (2004a), where the macroscopic deformation gradient tensor was incorporated into the kinematical macro–micro scale transition. More specifically, a second-gradient continuum was employed at the macro-scale, while a classical Cauchy continuum was adopted at the RVE level. Afterwards, other second-order strategies were proposed in the literature following this approach. Kaczmarczyk et al. (2008) and Luscher et al. (2012) studied the enforcement boundary conditions on the RVE. Kouznetsova et al. (2004b) and Kaczmarczyk et al. (2010) addressed aspects of size effects in second-order computational homogenisation. Luscher et al. (2010) proposed a framework for hierarchical multi-scale modelling of materials, where a volumetric constraint was incorporated, implying the presence of body forces at the RVE level. Nguyen et al. (2013) explored the discontinuous Galerkin method to derive a strain-gradient formulation to model the macroscopic second-order continua. Lesičar et al. (2014, 2016) presented a two-scale homogenisation procedure using C^1 continuity macrolevel discretisation at small and large strains, respectively. Yvonnet et al. (2020) proposed a computational framework to model anisotropic strain-gradient effects in elastic structures. In the context of a variational approach, it is worth mentioning the work developed by Rodrigues Lopes and Andrade Pires (2022b,d,a) based on the Method of Multi-scale Virtual Power (Blanco et al., 2016a,b), where the volumetric constraint was also considered in the formulation. Hii and El Said (2022) extended the second-order homogenisation for application to thick shell models, in which a novel constraint was proposed to downscale transverse shear strain properly. Moreover, fully second-order homogenisation approaches have been developed to improve the standard second-order computational homogenisation schemes. For instance, Lesičar et al. (2017) presented a second-order computational homogenisation scheme employing the nonlocal theory at both micro- and macro-scales. Rodrigues Lopes and Andrade Pires (2022c) proposed a homogenisation-based multi-scale model at finite strains, linking the micro-scale to the macro-scale level through a second-gradient constitutive theory. In addition, Schmidt et al. (2022) developed a computational homogenisation framework for investigating higher-order continua, incorporating first-, second-, and third-order effects at both micro- and macro-scales.

Recent research in the field of second-order computational homogenisation has explored various aspects of metamaterials and architected materials, including cellular and lattice structures. Nguyen and Noels (2014) explored a second-order multi-scale computational homogenisation approach to study cellular materials, including aspects of instability phenomena and strain localisation. Weeger (2021) presented a numerical homogenisation method for computing the effective second gradient constitutive models of cubic beam-lattice metamaterials. Wu et al. (2023) proposed a second-order computational homogenisation

enhanced with non-uniform body forces for modelling non-linear cellular materials and metamaterials. Furthermore, Molavitabrizi et al. (2023) developed a computational homogenisation scheme based on a second-order strain gradient theory (or Mindlin elasticity theory) to investigate three-dimensional lattice materials, in which numerical modelling is confronted with experimental tests.

More recently, Dos Santos et al. (2023) proposed a new formulation based on second-order computational homogenisation at finite strains for multi-scale modelling of natural and architected materials in the presence of voids. A second gradient theory describes the macro-scale continuum, and the micro-scale is modelled by the concept of Representative Volume Element (RVE) with the classical first-order continuum mechanics. The kinematics was defined only in the solid domain of the RVE, and a new expression for the homogenisation of the second-order gradient was postulated, allowing the consideration of voids inside the RVE and its outer boundary. In the light of variational formulations, the framework based on the Method of Multi-scale Virtual Power provided the construction of three different sets of micro-scale kinematic constraints over the RVE: minimal (lower bound), periodic, and direct (upper bound). The finite element solution of the discrete equilibrium problem was also carefully described in detail, encompassing some implementation considerations.

Therefore, from the previous discussion and arguments, it is imperative to develop enhanced continuum models that can effectively capture the unique characteristics of artificial materials, especially those displaying specific and exotic features, as well as high-order effects. In this study, we investigate the robustness and applicability of a multi-scale second-order computational homogenisation approach, recently introduced by Dos Santos et al. (2023), to analyse the macroscopic behaviour of mechanical meta-materials and architected materials. It is worth mentioning that second-order approaches at finite strains are particularly interesting for capturing higher strain gradients and high curvatures, as well as second-order deformation modes (e.g., bending and torsion) and coupling deformation mechanisms. Moreover, a characteristic length scale parameter is naturally embedded in the formulation, allowing the investigation of size effects with respect to the RVE length.

Several coupled multi-scale numerical examples are addressed in the present contribution through the so-called FE^2 framework, i.e., finite element simulations at both macro- and micro-scales. Initially, a designed geometric arrangement is studied for the internal architecture of a novel metamaterial with induced undulation effects by tension or compression. This unprecedented behaviour provides new insights to design structures for shape-shifting applications in architected robotic metamaterials. Afterwards, two- and three-dimensional architected materials under bending are simulated. Still, in the context of metamaterials, an example related to compression-induced torsion is discussed. Furthermore, comparisons with first-order multi-scale theory and DNS models are performed for all numerical examples.

The outline of the paper is organised as follows. Section 2 summarises the multi-scale second-order homogenisation formulation based on the Method of the Multi-scale Virtual Power for modelling natural and architected materials in the presence of voids. Section 3 presents several challenging numerical examples to assess the predictive capability of the multi-scale second-order homogenisation strategy to capture second-order effects in mechanical metamaterials and architected structures. Finally, the main conclusions and remarks are reported in Section 4.

2. A second-order computational homogenisation-based formulation for RVEs containing voids

The multi-scale framework based on second-order computational homogenisation recently proposed by Dos Santos et al. (2023) for investigating natural and architected materials in the presence of voids is summarised in the present section. As shown in Fig. 1, the macro-scale continuum (characteristic length L) is described by a second gradient theory, while the micro-scale or RVE (characteristic length l_μ) is governed by a first gradient continuum mechanics. In the proposed framework, the macroscopic deformation gradient $\boldsymbol{F}$ and the second gradient of the displacements $\mathbf{G}$ are inserted in the micro-scale model. After solving the micro-scale equilibrium problem, the homogenisation procedure allows us to recover the respective conjugate stresses accounted for the deformation descriptors in the strain energy density function at the macro-scale, i.e., the first Piola–Kirchhoff stress tensor $\boldsymbol{P}$ (associated with $\boldsymbol{F}$) and the higher-order stress tensor $\mathbf{Q}$ (related to $\mathbf{G}$). Furthermore, respective consistent tangents also need to be obtained for the coupled multi-scale analysis.

The approach is established based on the *Method of the Multi-Scale Virtual Power* (Blanco et al., 2016a,b), in which a variationally consistent formulation is developed to derive RVE-based multi-scale models for second-order continua.

2.1. Multi-scale kinematics

Consider the RVE of a porous solid presented in Fig. 2. The total domain Ω_μ is composed of the solid portion Ω_μ^s and the voids portion Ω_μ^v, i.e.,

$$\Omega_\mu = \Omega_\mu^s \bigcup \Omega_\mu^v. \tag{1}$$

The outer boundary of the RVE, denoted by $\partial\Omega_\mu$, is given by

$$\partial\Omega_\mu = \partial\Omega_\mu^{s,b} \bigcup \partial\Omega_\mu^{v,b}, \tag{2}$$

where $\partial\Omega_\mu^{s,b}$ represents the outer boundary of the solid part and $\partial\Omega_\mu^{v,b}$ is the outer boundary of the porous portion.

Still, regarding the nomenclature for the boundaries, $\partial\Omega_\mu^{s,v}$ indicates the boundary of the voids. Thus, the boundary of the solid portion $\partial\Omega_\mu^s$ is given by

$$\partial\Omega_\mu^s = \partial\Omega_\mu^{s,b} \bigcup \partial\Omega_\mu^{s,v}. \tag{3}$$

Finally, the outer boundary of the solid part $\partial\Omega_\mu^{s,b}$ is calculated as

$$\partial\Omega_\mu^{s,b} = \partial\Omega_\mu^s \bigcap \partial\Omega_\mu. \tag{4}$$

2.1.1. Kinematic insertion

For second-order computational homogenisation approaches, an expression based on Taylor's expansion of the macro-scale displacement field, truncated in the second derivatives, is often adopted to approximate the micro-scale displacement. In this context, the micro-scale displacement $\boldsymbol{u}_\mu$ is composed of:

$$\boldsymbol{u}_\mu(\boldsymbol{Y}) = \boldsymbol{u}_M + (\boldsymbol{F} - \boldsymbol{I}) \cdot \boldsymbol{Y} + \frac{1}{2}\mathbf{G} : (\boldsymbol{Y} \otimes \boldsymbol{Y} - \boldsymbol{J}) + \tilde{\boldsymbol{u}}(\boldsymbol{Y}), \quad \forall \boldsymbol{Y} \in \Omega_\mu^s, \tag{5}$$

where $\boldsymbol{Y}$ is the vector of RVE reference coordinates, $\boldsymbol{u}_M$ indicates the macroscopic displacement and $\tilde{\boldsymbol{u}}$ denotes the micro-scale displacement fluctuation field. Since the present work deals with materials with voids, the kinematic insertion is only defined for the solid domain.

The additional term related to $\boldsymbol{J}$ was proposed by Blanco et al. (2016b) and denotes the second-order moment of volume tensor:

$$\boldsymbol{J} = \frac{1}{V_\mu^s} \int_{\Omega_\mu^s} \boldsymbol{Y} \otimes \boldsymbol{Y} dV, \tag{6}$$

where $V_\mu^s = \left|\Omega_\mu^s\right|$ is the volume of the solid domain Ω_μ^s.

Furthermore, the origin of the micro coordinate system can be conveniently located at the centroid of the solid part of the RVE, such that:

$$\int_{\Omega_\mu^s} \boldsymbol{Y} dV = \mathbf{0}. \tag{7}$$

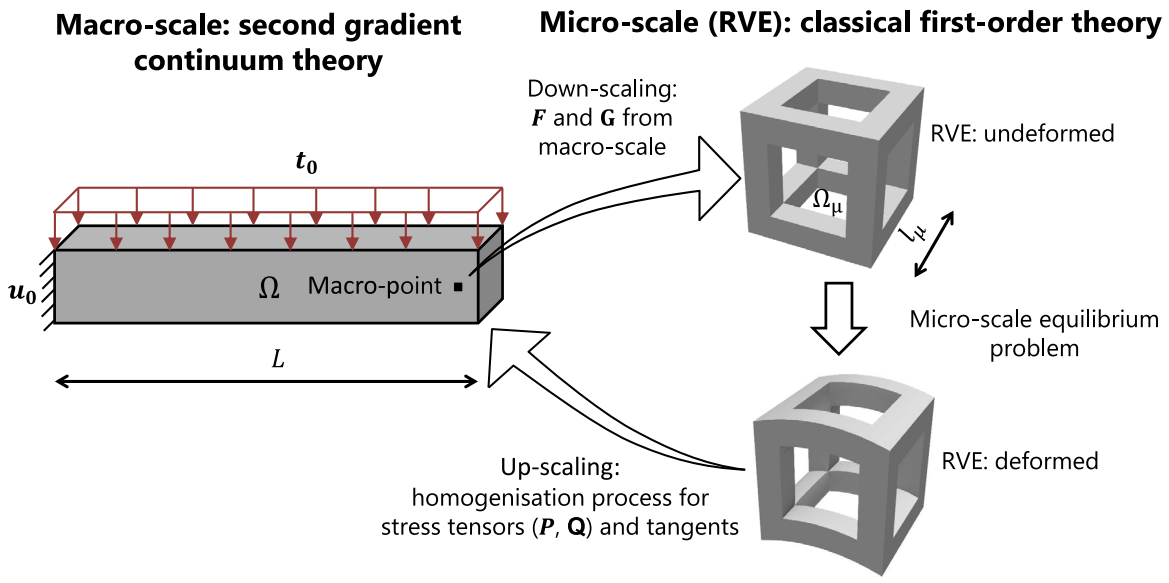

Fig. 1. Schematic representation of a multi-scale analysis based on second-order homogenisation, where $\boldsymbol{t}_0$ and $\boldsymbol{u}_0$ are the boundary conditions related to imposed traction and displacement, respectively.

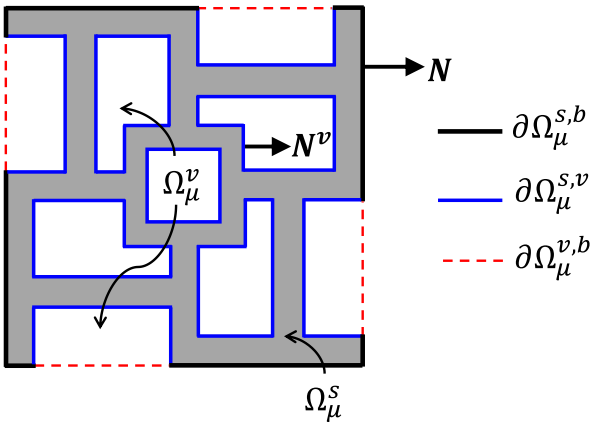

Fig. 2. RVE of an architected material with the representation of different types of domains, in which $\boldsymbol{N}$ is the normal at the outer RVE boundary and $\boldsymbol{N}^v$ is the normal at the void boundaries.

2.1.2. Kinematic homogenisation

The kinematic homogenisation procedure establishes how macro-scale kinematical descriptors ($\boldsymbol{u}_M$, $\boldsymbol{F}$ and $\mathbf{G}$) are recovered based on the volume averaging of the micro-scale kinematic quantities.

The homogenisation related to the macro-scale displacement vector is given by (Rocha et al., 2018; Blanco et al., 2023):

$$\boldsymbol{u}_M = \frac{1}{V_\mu^s}\int_{\Omega_\mu^s} \boldsymbol{u}_\mu dV. \tag{8}$$

The homogenisation formula related to the first macro-deformation gradient is defined as (Rocha et al., 2018; Blanco et al., 2023):

$$\boldsymbol{F} = \frac{1}{V_\mu^s}\left[\int_{\Omega_\mu^s} \boldsymbol{F}_\mu dV - \int_{\partial\Omega_\mu^{s,v}} \tilde{\boldsymbol{u}} \otimes \boldsymbol{N}^v dA - \int_{\partial\Omega_\mu^{s,b}} \tilde{\boldsymbol{u}} \otimes \bar{\boldsymbol{N}} dA\right], \tag{9}$$

with $\boldsymbol{N}^v$ denoting the normal unit vector on the void inner boundary (see the illustrative scheme in Fig. 2), and $\bar{\boldsymbol{N}}$ denoting a constant mean normal in the solid part of the RVE boundary $\partial\Omega_\mu^{s,b}$:

$$\bar{\boldsymbol{N}} = \frac{1}{A_\mu^{s,b}}\int_{\partial\Omega_\mu^{s,b}} \boldsymbol{N} dA. \tag{10}$$

The homogenisation formula for the second gradient is written as (Dos Santos et al., 2023):

$$\mathbf{G} = \frac{1}{V_\mu^s}\left[\int_{\Omega_\mu^s} \nabla_Y \boldsymbol{u}_\mu \otimes \boldsymbol{Y}\cdot\boldsymbol{J}^{-1} dV - \int_{\partial\Omega_\mu^{s,v}} \tilde{\boldsymbol{u}} \otimes \boldsymbol{N}^v \otimes \boldsymbol{Y}\cdot\boldsymbol{J}^{-1} dA - \int_{\partial\Omega_\mu^{s,b}} \tilde{\boldsymbol{u}} \otimes \bar{\bar{\boldsymbol{X}}}\cdot\boldsymbol{J}^{-1} dA\right], \tag{11}$$

with $\bar{\bar{\boldsymbol{X}}}$ given by

$$\bar{\bar{\boldsymbol{X}}} = \frac{1}{A_\mu^{s,b}}\int_{\partial\Omega_\mu^{s,b}} \boldsymbol{N}\otimes\boldsymbol{Y} dA - \frac{1}{A_\mu^{s,b}} V^s \boldsymbol{I}. \tag{12}$$

In Eqs. (9) and (11), the constant vector $\bar{\boldsymbol{N}}$ and second-order tensor $\bar{\bar{\boldsymbol{X}}}$, respectively, avoid spurious macro-scale gradients when considering a constant displacement fluctuation field (i.e., $\tilde{\boldsymbol{u}} = \boldsymbol{c}$) in the modelling of materials with random voids reaching the RVE boundary.

2.1.3. Kinematic admissibility

The kinematic admissibility provides the compatibility between kinematic insertion and kinematic homogenisation, which results in constraints that must be imposed at the RVE level. In this context, the compatibility between Eqs. (5) and (8) ensures the conservation of the displacement field, resulting in the volumetric constraint:

$$\int_{\Omega_\mu^s} \tilde{\boldsymbol{u}} dV = \boldsymbol{0}. \tag{13}$$

The kinematic admissibility for the deformation gradient (compatibility between Eqs. (5) and (9)) results in a constraint on the outer solid boundary:

$$\int_{\partial\Omega_\mu^{s,b}} \tilde{\boldsymbol{u}} \otimes \left(\boldsymbol{N} - \bar{\boldsymbol{N}}\right) dA = \boldsymbol{0}. \tag{14}$$

Similarly, the kinematic homogenisation for the second deformation gradient (Eq. (11)), taking into account the micro-scale displacement field (Eq. (5)), leads to the additional boundary condition:

$$\int_{\partial\Omega_\mu^{s,b}} \tilde{\boldsymbol{u}} \otimes \left(\boldsymbol{N}\otimes\boldsymbol{Y} - \bar{\bar{\boldsymbol{X}}}\right)\cdot\boldsymbol{J}^{-1} dA = \boldsymbol{0} \Leftrightarrow \int_{\partial\Omega_\mu^{s,b}} \tilde{\boldsymbol{u}} \otimes \left(\boldsymbol{N}\otimes\boldsymbol{Y} - \bar{\bar{\boldsymbol{X}}}\right) dA = \boldsymbol{0}, \tag{15}$$

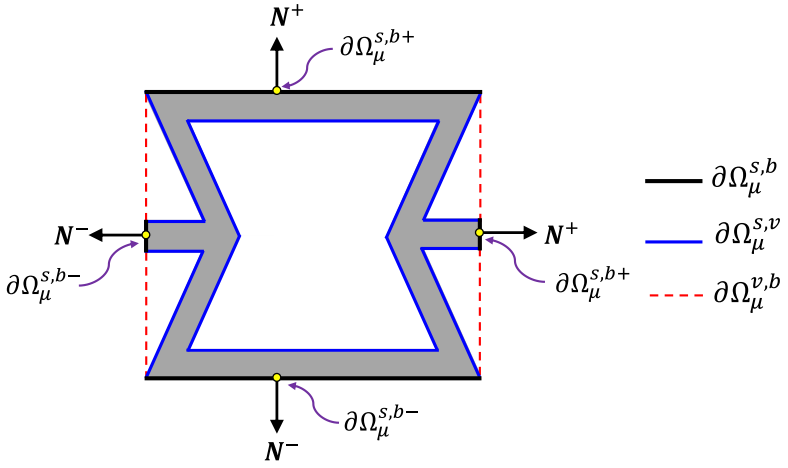

Fig. 3. Illustrative representation of a periodic porous material.

2.2. Sets of admissible fluctuations

The space of kinematically admissible RVE displacement fluctuation fields allows us to derive classes of multi-scale models. Thus, three second-order multi-scale models are defined based on specific sets of kinematically admissible fluctuations: (i) minimal constraint (lower bound), (ii) periodic constraint, and (iii) direct constraint (upper bound).

2.2.1. Sets of admissible fluctuations for minimal constraint

Let us define $\tilde{\mathcal{V}}$ as the set of admissible fluctuation displacements that satisfies the constraints of Eqs. (13) to (15), such that $\tilde{\boldsymbol{u}} \in \tilde{\mathcal{V}}$ and $\delta\tilde{\boldsymbol{u}} \in \tilde{\mathcal{V}}$:

$$\tilde{\mathcal{V}} = \left\{ \tilde{\boldsymbol{u}} \text{ sufficiently regular in } \Omega_\mu^s, \int_{\partial\Omega_\mu^{s,b}} \tilde{\boldsymbol{u}} \otimes \left(\boldsymbol{N} - \bar{\boldsymbol{N}}\right) dA = \boldsymbol{0}, \right. \\ \left. \int_{\partial\Omega_\mu^{s,b}} \tilde{\boldsymbol{u}} \otimes \left(\boldsymbol{N} \otimes \boldsymbol{Y} - \bar{\bar{\boldsymbol{X}}}\right) dA = \boldsymbol{0}, \int_{\Omega_\mu^s} \tilde{\boldsymbol{u}} dV = \boldsymbol{0} \right\}. \tag{16}$$

i.e., the set of minimally constrained displacement fluctuation fields, where the kinematical relations between both macro- and micro-scales are satisfied.

2.2.2. Sets of admissible fluctuations for periodic constraint

Further constraints can be incorporated into the RVE kinematics as subsets of solutions that still satisfy the kinematic admissibility. In this context, the periodic boundary condition is defined as

$$\tilde{\boldsymbol{u}}^+ = \tilde{\boldsymbol{u}}^- \Leftrightarrow \tilde{\boldsymbol{u}}\left(\boldsymbol{Y}^+\right) = \tilde{\boldsymbol{u}}\left(\boldsymbol{Y}^-\right), \quad \forall \boldsymbol{Y}^+ \in \partial\Omega_\mu^{s,b+}, \ \forall \boldsymbol{Y}^- \in \partial\Omega_\mu^{s,b-}, \tag{17}$$

with + and − denoting opposite RVE boundaries, i.e., $\partial\Omega_\mu^{s,b+} = \partial\Omega_\mu^{s,b} \bigcap \partial\Omega_\mu^{+}$ and $\partial\Omega_\mu^{s,b-} = \partial\Omega_\mu^{s,b} \bigcap \partial\Omega_\mu^{-}$. Moreover, the unit normal vectors of opposite faces must obey the following expression:

$$\boldsymbol{N}\left(\boldsymbol{Y}^+\right) = -\boldsymbol{N}\left(\boldsymbol{Y}^-\right), \quad \forall \boldsymbol{Y}^+ \in \partial\Omega_\mu^{s,b+}, \ \forall \boldsymbol{Y}^- \in \partial\Omega_\mu^{s,b-}. \tag{18}$$

This boundary condition is appropriate to describe the behaviour of materials with periodic microstructure. When voids reach the outer boundary of the RVE, the periodic condition is only applied if the voids are positioned in a periodic manner on opposite faces of the RVE (see Fig. 3). In this particular case, the mean normal $\bar{\boldsymbol{N}}$ is null by definition and $\bar{\bar{\boldsymbol{X}}}$ vanishes in the problem with periodic boundary conditions due to being a constant tensor (see more details in Dos Santos et al. (2023)). Consequently, Eq. (14) is automatically satisfied with the periodic constraint.

In particular, the incorporation of the periodic condition for RVEs with rectangular or cubic shapes (cases in which the normal vector is constant on each surface) in Eq. (15) results in:

$$\int_{\partial\Omega_\mu^{s,b+(j)}} \tilde{u}_i dA = 0. \tag{19}$$

for each positive surface j.

Therefore, the set of admissible fluctuations for the periodic boundary condition is composed of

$$\tilde{\mathcal{V}}^{per} = \left\{ \tilde{\boldsymbol{u}} \text{ sufficiently regular in } \Omega_\mu^s, \ \tilde{\boldsymbol{u}}\left(\boldsymbol{Y}^+\right) = \tilde{\boldsymbol{u}}\left(\boldsymbol{Y}^-\right), \int_{\Omega_\mu^s} \tilde{\boldsymbol{u}} dV = \boldsymbol{0}, \right. \\ \left. \int_{\partial\Omega_\mu^{s,b+(i)}} \tilde{\boldsymbol{u}} dA = \boldsymbol{0}, \text{ for each positive surface } i \right\}. \tag{20}$$

2.2.3. Sets of admissible fluctuations for direct constraint

Null fluctuations on the RVE boundary can also be defined as subsets of solutions that satisfy the kinematic admissibility. Thus, the direct boundary condition emerges as

$$\tilde{\boldsymbol{u}}\left(\boldsymbol{Y}\right) = \boldsymbol{0}, \quad \forall \boldsymbol{Y} \in \partial\Omega_\mu^{s,b}. \tag{21}$$

Thus, the set of admissible solutions for the direct constraint is given by

$$\tilde{\mathcal{V}}^{dir} = \left\{ \tilde{\boldsymbol{u}} \text{ sufficiently regular in } \Omega_\mu^s, \ \tilde{\boldsymbol{u}}\left(\boldsymbol{Y}\right) = \boldsymbol{0}, \ \forall \boldsymbol{Y} \in \partial\Omega_\mu^{s,b}, \right. \\ \left. \int_{\Omega_\mu^s} \tilde{\boldsymbol{u}} dV = \boldsymbol{0} \right\}. \tag{22}$$

Finally, we can conclude that $\tilde{\mathcal{V}}^{dir} \subset \tilde{\mathcal{V}}^{per} \subset \tilde{\mathcal{V}}$. Therefore, the solutions obtained with direct and periodic boundary conditions respect the minimal kinematic admissible constraint (i.e., least kinematically constrained).

2.3. Principle of multi-scale virtual power

The *Principle of Multi-scale Virtual Power* (PMVP) is employed to ensure the conservation of the virtual power in the scale transition. In particular, a dual formulation based on the Lagrange multiplier method is explored to define the PMVP. Some advantages of this approach are: (i) the Lagrange multipliers allow us to understand the reactive nature of kinematic constraints, and (ii) the Lagrange multipliers can be used to recover the homogenised stresses. Moreover, Rodrigues Lopes et al.

(2021) showed that the Lagrange multipliers method could be computationally efficient to enforce micro-scale constraints in the context of multi-scale modelling based on computational homogenisation.

For the particular case of the minimal constraint, whose set of admissible fluctuations is defined in Eq. (16), the PMVP can be expressed by

$$\begin{aligned}\boldsymbol{P} : \delta\boldsymbol{F} + \mathbf{Q} \vdots \delta\mathbf{G} = \frac{1}{V_\mu}\Bigg[&\int_{\Omega_\mu^s} \boldsymbol{P}_\mu : \left(\delta\boldsymbol{F} + \delta\mathbf{G}\cdot\boldsymbol{Y} + \nabla_Y \delta\tilde{\boldsymbol{u}}\right) dV \\ &-\delta\lambda_L : \left(\int_{\partial\Omega_\mu^{s,b}} \tilde{\boldsymbol{u}} \otimes \left(\boldsymbol{N} - \bar{\boldsymbol{N}}\right) dA\right) \\ &-\lambda_L : \left(\int_{\partial\Omega_\mu^{s,b}} \delta\tilde{\boldsymbol{u}} \otimes \left(\boldsymbol{N} - \bar{\boldsymbol{N}}\right) dA\right) \\ &-\delta\lambda_{\mathbf{M}} \vdots \left(\int_{\partial\Omega_\mu^{s,b}} \tilde{\boldsymbol{u}} \otimes \left(\boldsymbol{N}\otimes\boldsymbol{Y} - \bar{\bar{\boldsymbol{X}}}\right) dA\right) \\ &-\lambda_{\mathbf{M}} \vdots \left(\int_{\partial\Omega_\mu^{s,b}} \delta\tilde{\boldsymbol{u}} \otimes \left(\boldsymbol{N}\otimes\boldsymbol{Y} - \bar{\bar{\boldsymbol{X}}}\right) dA\right) \\ &- \int_{\Omega_\mu^s} \delta\lambda_V \cdot \tilde{\boldsymbol{u}} dV - \int_{\Omega_\mu^s} \lambda_V \cdot \delta\tilde{\boldsymbol{u}} dV\Bigg], \\ &\forall \left(\delta\boldsymbol{F}, \delta\mathbf{G}, \delta\tilde{\boldsymbol{u}}, \delta\lambda_L, \delta\lambda_{\mathbf{M}}, \delta\lambda_V\right),\end{aligned} \tag{23}$$

where the Lagrange multipliers λ_V, λ_L and $\lambda_{\mathbf{M}}$ enforce the constraints defined by Eqs. (13)–(15), respectively.

Similar expressions are defined for the cases of the periodic and direct constraints. More details can be found in Dos Santos et al. (2023).

2.3.1. Micro-scale equilibrium problem

The weak micro-equilibrium equation is derived from the PMVP, by setting $\delta\boldsymbol{F} = \mathbf{0}$ and $\delta\mathbf{G} = \mathbf{0}$. For the minimal constraint, it is expressed by:

$$\begin{aligned}&\int_{\Omega_\mu^s} \boldsymbol{P}_\mu : \nabla_Y \delta\tilde{\boldsymbol{u}} dV \\ &- \delta\lambda_L : \left(\int_{\partial\Omega_\mu^{s,b}} \tilde{\boldsymbol{u}} \otimes \left(\boldsymbol{N} - \bar{\boldsymbol{N}}\right) dA\right) \\ &-\lambda_L : \left(\int_{\partial\Omega_\mu^{s,b}} \delta\tilde{\boldsymbol{u}} \otimes \left(\boldsymbol{N} - \bar{\boldsymbol{N}}\right) dA\right) \\ &-\delta\lambda_{\mathbf{M}} \vdots \left(\int_{\partial\Omega_\mu^{s,b}} \tilde{\boldsymbol{u}} \otimes \left(\boldsymbol{N}\otimes\boldsymbol{Y} - \bar{\bar{\boldsymbol{X}}}\right) dA\right) \\ &-\lambda_{\mathbf{M}} \vdots \left(\int_{\partial\Omega_\mu^{s,b}} \delta\tilde{\boldsymbol{u}} \otimes \left(\boldsymbol{N}\otimes\boldsymbol{Y} - \bar{\bar{\boldsymbol{X}}}\right) dA\right) \\ &- \delta\lambda_V \cdot \int_{\Omega_\mu^s} \tilde{\boldsymbol{u}} dV - \lambda_V \cdot \int_{\Omega_\mu^s} \delta\tilde{\boldsymbol{u}} dV = \mathbf{0} \quad \forall \left(\delta\tilde{\boldsymbol{u}}, \delta\lambda_L, \delta\lambda_{\mathbf{M}}, \delta\lambda_V\right).\end{aligned} \tag{24}$$

2.3.2. Homogenised stress tensors and consistent tangents

In general, the first Piola–Kirchhoff stress and the homogenised higher-order stress tensors are obtained by volume averaging through:

$$\boldsymbol{P} = \frac{1}{V_\mu}\int_{\Omega_\mu^s} \boldsymbol{P}_\mu dV, \tag{25}$$

and

$$\mathbf{Q} = \frac{1}{V_\mu}\int_{\Omega_\mu^s} \left(\boldsymbol{P}_\mu \otimes \boldsymbol{Y}\right)^S dV, \tag{26}$$

where $\bullet^S$ denotes the right-hand symmetry operator.

For each of the sets of admissible fluctuations, the homogenised stress tensors can also be expressed in terms of the Lagrange multipliers employed to enforce the corresponding constraints. This fact is particularly interesting for a more efficient computation of the homogenised stresses and of the consistent macroscopic tangents. The finite element method is employed to solve the discrete form of the multi-scale problem, encompassing the Newton–Raphson scheme for the iterative solution of the corresponding non-linear systems of equations at both scales. Therefore, the homogenised consistent tangents ($\mathbf{A}$, $\mathbf{A}_\mathbf{G}$, $\mathbf{H}$ and $\mathbf{H}_F$) must be defined to solve the non-linear macroscopic equilibrium problem with the Newton–Raphson scheme:

$$\mathbf{A} = \frac{\partial \boldsymbol{P}}{\partial \boldsymbol{F}}, \tag{27}$$

$$\mathbf{A}_\mathbf{G} = \frac{\partial \boldsymbol{P}}{\partial \mathbf{G}}, \tag{28}$$

$$\mathbf{H} = \frac{\partial \mathbf{Q}}{\partial \mathbf{G}}, \tag{29}$$

$$\mathbf{H}_F = \frac{\partial \mathbf{Q}}{\partial \boldsymbol{F}}. \tag{30}$$

Further details of the computational implementation for FE^2 simulations are described in Dos Santos et al. (2023).

3. Numerical examples

In what follows, several coupled multi-scale numerical examples of mechanical metamaterials and architected materials are presented to show the applicability and robustness of the second-order computational strategy. For all numerical examples, the results of multi-scale simulations based on second-order homogenisation are compared with the responses provided by Direct Numerical Simulations (DNS) and first-order homogenisation theory. Multi-scale simulations are conducted in the context of the FE^2 framework, i.e., finite element analyses at both macro and micro-scales. To comply with the C^1-continuity requirement, mixed finite elements were employed at the macro-scale (see more details in Rodrigues Lopes and Andrade Pires (2022d)). Different lengths for RVEs (multi-scale simulations) and unit cells (DNS simulations) are defined to assess the impact of the size effect on the global mechanical behaviour of the investigated structures. Mesh convergence studies are conducted in the context of multi-scale simulations to verify the appropriate mesh refinement for modelling each structural problem. Although the results are presented and discussed only for the macro-scale mesh refinement, convergence studies were also carried out for the micro-scale, resulting in the meshes selected for the RVE (multi-scale models) and the unit cells (DNS models). In this sense, mesh convergences are obtained both on the macro-scale and on the micro-scale, in which only the macro-scale results are presented. Furthermore, the simulated materials are assumed to have elastic constitutive behaviour.

3.1. Numerical example 1: novel metamaterial with tension/compression-induced undulation

The first numerical example aims to investigate a new design for a mechanical metamaterial, which displays transverse undulation when subjected to tensile or compressive loading. This represents an exotic behaviour that is significantly different from what is observed in conventional materials. To the authors' best knowledge, this is the first time that a metamaterial of this type is examined. This new microstructure can be explored for shape-shifting applications in architected robotic metamaterials, for instance. The mechanical behaviour of this architected material is illustrated by two-dimensional finite element models, considering plane strain conditions. Regarding the elastic properties of the metamaterial, Young's modulus of $E = 210$ GPa and Poisson's ratio of $\nu = 0.3$ are assumed.

3.1.1. DNS models

Fig. 4 shows the unit cell geometry for the new metamaterial, along with the mesh that is composed of isoparametric 8-noded quadratic quadrilateral elements (Q8) with 4 integration points. DNS models are formed by periodic arrays based on the unit cell of Fig. 4. In this context, Fig. 5 presents three DNS models proposed to numerically simulate the new metamaterial: (i) DNS model 1 (20 × 8 unit cells),

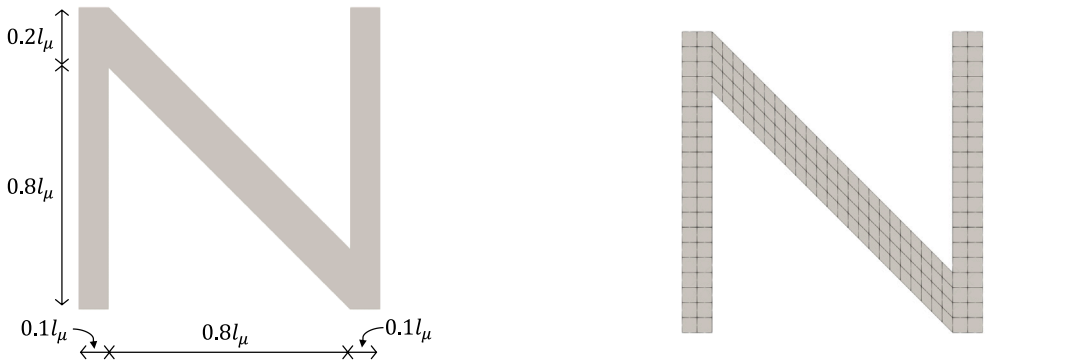

(a) Geometry.

(b) Mesh: 172 elements (Q8) and 643 nodes.

Fig. 4. Unit cell and RVE.

Table 1
Mesh of DNS models.

DNS	Elements (Q8)	Nodes
Model 1 - Size 1 (l_μ = 0.500 mm)	27 520	95 381
Model 2 - Size 2 (l_μ = 0.333 mm)	61 920	214 231
Model 3 - Size 3 (l_μ = 0.250 mm)	110 080	380 521

(ii) DNS model 2 (30 × 12 unit cells) and (iii) DNS model 3 (40 × 16 unit cells). It is worth mentioning that the macroscopic dimensions of the DNS models are the same. Thus, the unit cell size (l_μ) is different for each DNS model: (I) DNS model 1: l_μ = 1.000 mm, (II) DNS model 2: l_μ = 0.500 mm, and (iii) DNS model 3: l_μ = 0.250 mm. The material volume fraction is the same for all DNS models. Moreover, mesh data for the DNS models are presented in Table 1.

Regarding the boundary conditions of the DNS model, zero displacements are prescribed on the left side of the structure ($u_{0x} = u_{0y} = 0$). On the right side of the structure, zero displacements are prescribed vertically ($u_{0y} = 0$) and non-zero displacements are imposed horizontally ($u_{0x} \neq 0$) considering: (i) u_{0x} = 0.5 mm (loading programme associated with tension), and (ii) u_{0x} = −0.5 mm (loading programme associated with compression). The prescribed displacements are imposed in 10 equally-spaced increments.

The deformed configuration of the DNS models for the tensile and compressive loadings is shown in Figs. 6 and 7, respectively. Note that the new material has a tension/compression-induced undulation behaviour, which is a different response than expected for a natural material. Moreover, the shape of the induced vertical waves inverts, when comparing deformation induced by tension and compression. It must be noted that the size of the unit cell size has no significant influence on the maximum vertical displacements of the deformed structure. Therefore, this new metamaterial does not display significant size effects, concerning the microstructural size. Note that the loading programme associated with compression results in higher values for the maximum vertical displacement compared to the loading programme associated with tension.

3.1.2. Multi-scale simulations

The three boundary conditions derived from the second-order multi-scale formulation, introduced in Section 2.2, are imposed to investigate the new metamaterial: (I) second-order minimal constraint (2nd-order — Minimal) or lower bound, (II) second-order periodic constraint (2nd-order — Periodic), and (III) second-order direct constraint (2nd-order — Direct) or upper bound. For comparison purposes, three boundary conditions derived from the classical first-order multi-scale formulation (see Reis and Andrade Pires (2013)) were also investigated: (i) first-order uniform traction boundary condition (1st-order - Traction) or lower bound, (ii) first-order periodic boundary condition (1st-order — Periodic), and (iii) first-order linear boundary condition (1st-order Linear) or upper bound.

In the context of coupled multi-scale analyses, modelling aspects of the macro-scale (described by a second gradient theory) and the micro-scale (governed by a first gradient continuum mechanics) must be defined. As shown in Fig. 8, the geometry and boundary conditions of the structure at the macro-scale are consistent with the DNS model. For the simulations with second-order homogenisation, mixed quadrilateral finite elements (Q8F4L1) with 4 integration points were employed at macro-scale to comply with the C^1-continuity requirement (Rodrigues Lopes and Andrade Pires, 2022d). For first-order homogenisation, standard isoparametric elements with 8 nodes (Q8) and 4 integration points were used. This type of element was also employed at the RVE level, for both cases. The micro-scale is modelled by the RVE shown in Fig. 4. The geometry, boundary conditions and mesh of the RVE are the same as those defined for the unit cells of the DNS models. Hence, the loading programmes associated with tension (u_{0x} = 0.5 mm) and compression (u_{0x} = −0.5 mm) were imposed at the macro-scale to perform the multi-scale simulations.

In the first place, three macro-scale meshes were investigated in order to verify the convergence of results for multi-scale analyses. The RVE discretisation is kept consistent with the meshes employed in the DNS. The mesh data, including the number of elements and nodes, is presented in Fig. 9. The mesh refinement studies, performed for l_μ = 0.500 mm and based on the horizontal reaction force (F_x), are presented in Tables 2 and 3 for tension and compression loading programmes, respectively. To be more precise, F_x is determined by the sum of nodal horizontal reaction forces on the right side of the structure, where the displacement is imposed. Since the relative differences are small, there is no influence of the macroscopic discretisation in the obtained results. Therefore, mesh 1 is sufficient to perform the multi-scale analyses.

In the second place, three RVE lengths were investigated, corresponding to the unit cell sizes considered in the DNS simulations: l_μ = 0.500 mm, l_μ = 0.333 mm and l_μ = 0.250 mm. Figs. 10(a) and 10(b) show the comparison of the horizontal reactive force obtained with the multi-scale simulations (first- and second-order homogenisation) and the DNS models, considering axial tension and axial compression, respectively. For quantitative comparison purposes, Tables 4, 5, 6 and 7 show the relative differences (in modulus) of the multi-scale models compared to the respective DNS models. In order to contribute to the discussion of results, the deformed macroscopic meshes for the multi-scale models with l_μ = 0.50 mm are shown in Figs. 11 and 12. The multi-scale simulations also capture both the tension and compression-induced undulation for the novel metamaterial. Regarding simulations with second-order multi-scale models: (i) the periodic constraint provides results in close agreement with the DNS model, (ii)

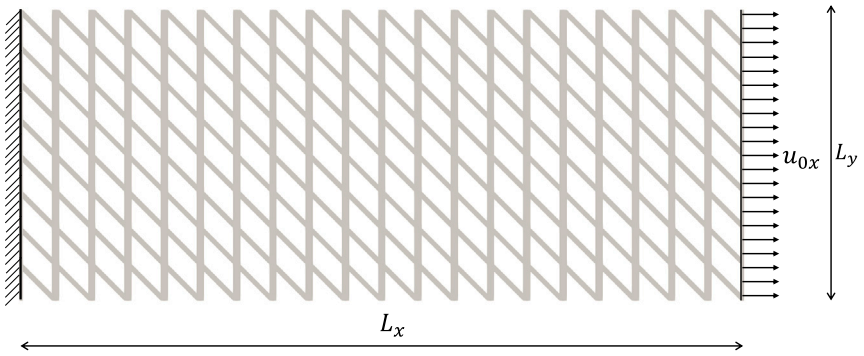

(a) DNS model 1 (20x8 unit cells): Size 1.

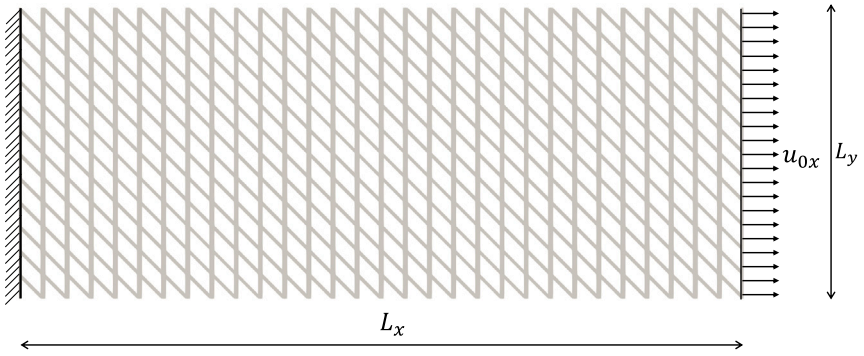

(b) DNS model 2 (30x12 unit cells): Size 2.

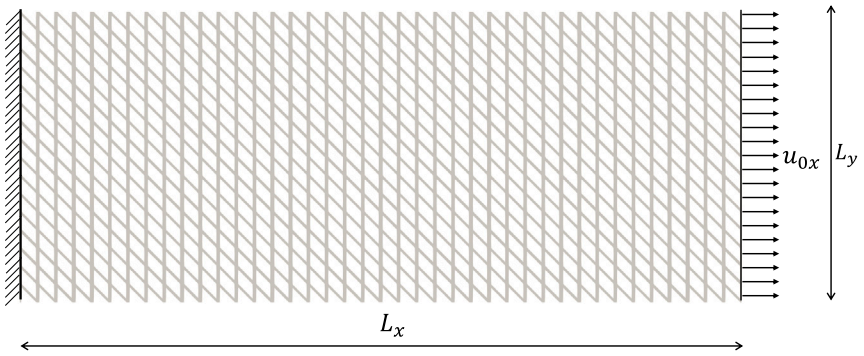

(c) DNS model 3 (40x16 unit cells): Size 3.

Fig. 5. Geometry of the DNS models (L_x = 10 mm and L_y = 4 mm).

Table 2
Mesh study for multi-scale analysis with RVE length 1 (l_μ = 0.500 mm) — loading programme associated with tension: mesh x reaction force (F_x).

	Reaction force F_x (N)				
	Mesh 1	Mesh 2	Mesh 3	Differences in module	
Multi-scale models	(1)	(2)	(3)	(2) to (1)	(3) to (2)
2nd-order: Minimal	102.58	101.82	101.67	0.75%	0.14%
2nd-order: Periodic	209.95	207.31	206.29	1.26%	0.49%
2nd-order: Direct	1469.22	1466.08	1464.92	0.21%	0.08%
1st-order: Uniform traction	91.57	89.90	89.14	1.82%	0.85%
1st-order: Periodic	196.69	193.91	192.59	1.42%	0.68%
1st-order: Linear	1462.73	1458.62	1456.75	0.28%	0.13%

the minimum constraint represents a lower bound, but keeping close to the model response DNS, (iii) the direct constraint results in an upper bound, i.e. the stiffest solution (most kinematically constrained), whose response has a significant difference when compared to DNS model. Furthermore, the previously described conclusions are analogous to first-order multi-scale simulations under the respective assumptions of: (I) periodic boundary condition, (II) uniform traction boundary condition, and (III) linear boundary condition. These observations are consistent with the maximum vertical displacement values obtained. The first- and second-order multi-scale models lead to similar values of the macroscopic reaction force, but the deformed macroscopic model is slightly affected by the selected formulation. Nonetheless, the periodic boundary conditions are the ones that result in maximum vertical displacements closer to the values obtained with the DNS.

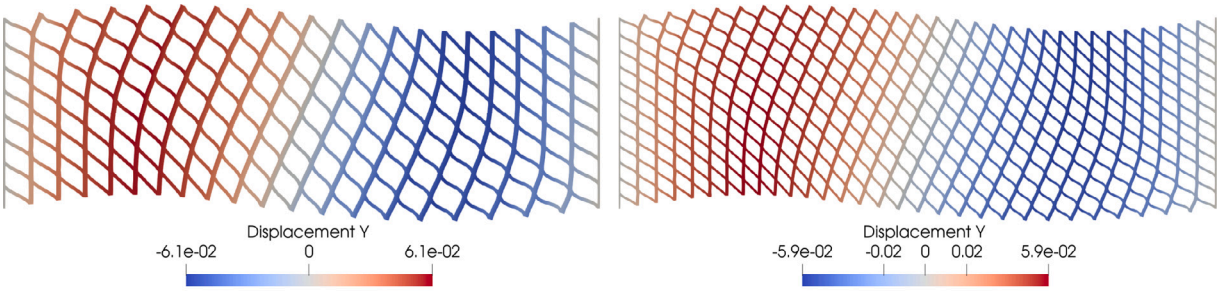

(a) DNS model 1 (20x8 unit cells). (b) DNS model 2 (30x12 unit cells).

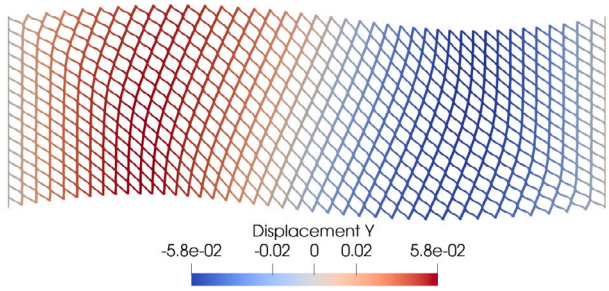

(c) DNS model 3 (40x16 unit cells).

Fig. 6. Vertical displacements in mm (scale factor = 4) for DNS models with loading programme related to axial tension.

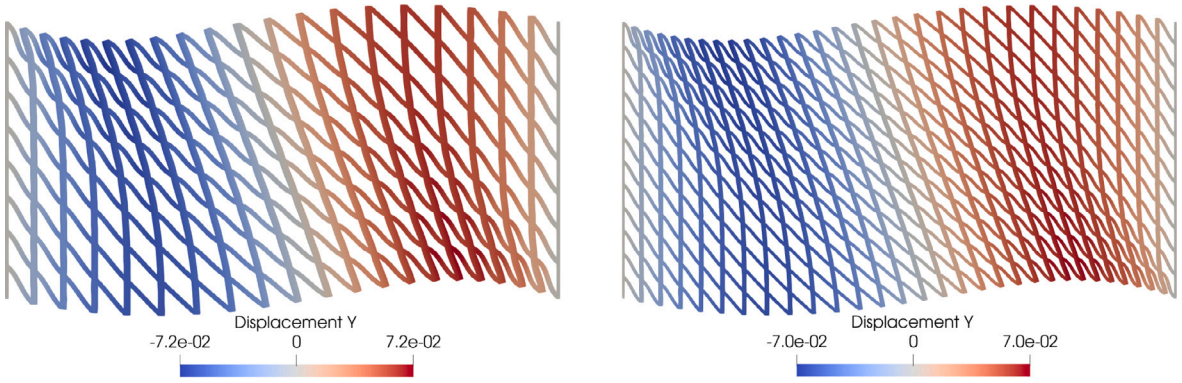

(a) DNS model 1 (20x8 unit cells). (b) DNS model 2 (30x12 unit cells).

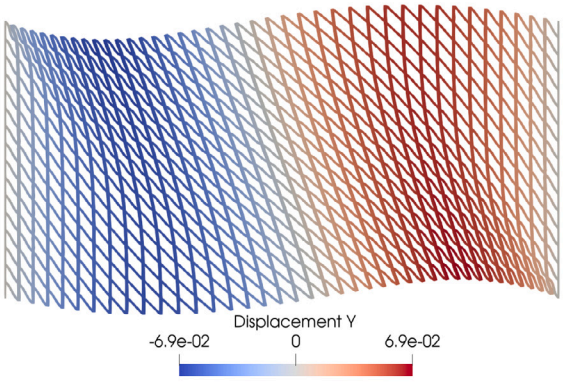

(c) DNS model 3 (40x16 unit cells).

Fig. 7. Vertical displacements in mm (scale factor = 4) for DNS models with loading programme related to axial compression.

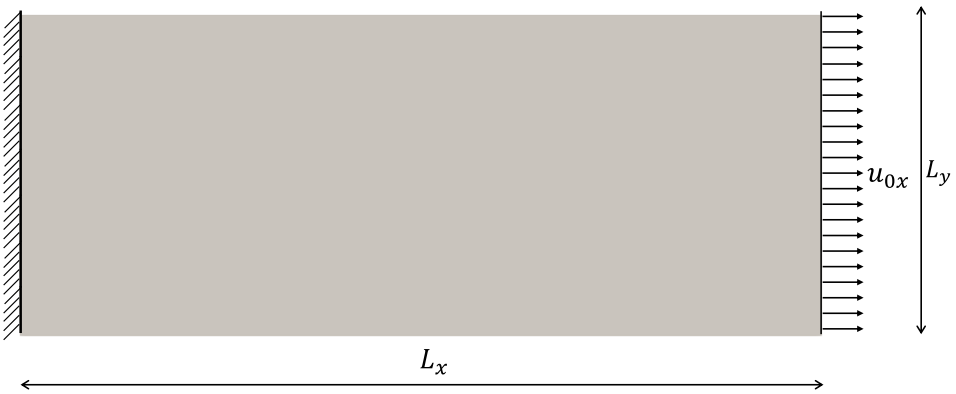

Fig. 8. Geometry and boundary conditions (L_x = 10 mm and L_y = 4 mm).

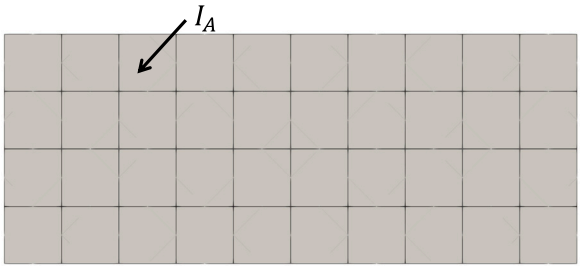

(a) Mesh 1: 40 elements (Q8F4L1) and 149 nodes.

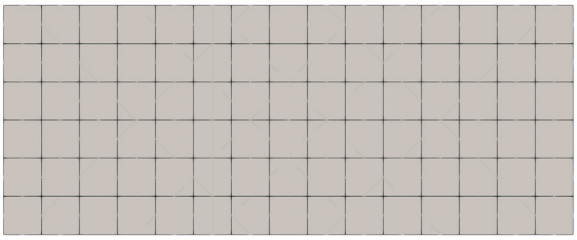

(b) Mesh 2: 90 elements (Q8F4L1) and 313 nodes.

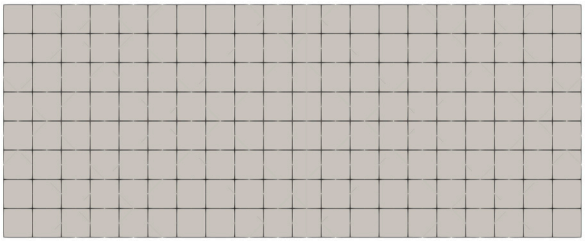

(c) Mesh 3: 160 elements (Q8F4L1) and 537 nodes.

Fig. 9. Macro-scale meshes.

Table 3
Mesh study for multi-scale analysis with RVE length 1 (l_μ = 0.500 mm) — loading programme associated with compression: mesh x reaction force (F_x).

	Reaction force F_x (N)				
	Mesh 1	Mesh 2	Mesh 3	Differences in module	
Multi-scale models	(1)	(2)	(3)	(2) to (1)	(3) to (2)
2nd-order: Minimal	−94.08	−93.07	−92.71	1.07%	0.39%
2nd-order: Periodic	−185.06	−183.25	−182.57	0.98%	0.37%
2nd-order: Direct	−1409.28	−1407.64	−1407.08	0.12%	0.04%
1st-order: Uniform traction	−81.22	−79.98	−79.43	1.52%	0.69%
1st-order: Periodic	−172.00	−170.24	−169.44	1.02%	0.48%
1st-order: Linear	−1401.71	−1399.46	−1398.46	0.16%	0.07%

3.1.3. Analysis of the homogenised properties

The initial consistent tangents are interesting to understand better the axial tension/compression-induced undulation for the new metamaterial. The coupling-tangents $\mathbf{A_G}$ and $\mathbf{H}_F$, which couple first and second-order deformation modes, have null values for all components in this numerical example. Therefore, the observed mechanical behaviour is not a consequence of that kind of coupling, and that is the reason why first-order homogenisation is able to capture the undulation. Alternatively, the consistent tangent $\mathbf{A}$, which associates $\boldsymbol{P}$ with $\boldsymbol{F}$, is assessed to understand better the coupling mechanism that characterises this metamaterial.

For two-dimensional problems, the classical constitutive law for a homogeneous isotropic material can be written in simplified form as (Rodrigues Lopes and Andrade Pires, 2022d):

$$\begin{bmatrix} P_{11} \\ P_{21} \\ P_{12} \\ P_{22} \end{bmatrix} = \begin{bmatrix} \lambda+2\mu & 0 & 0 & \lambda \\ 0 & \mu & \mu & 0 \\ 0 & \mu & \mu & 0 \\ \lambda & 0 & 0 & \lambda+2\mu \end{bmatrix} \begin{bmatrix} F_{11}-1 \\ F_{21} \\ F_{12} \\ F_{22}-1 \end{bmatrix}, \tag{31}$$

where μ and λ are the Lamé parameters.

For multi-scale analysis, the initial version for the consistent tangent $\mathbf{A}$ is equivalent to the homogenised elastic constitutive tensor indicated

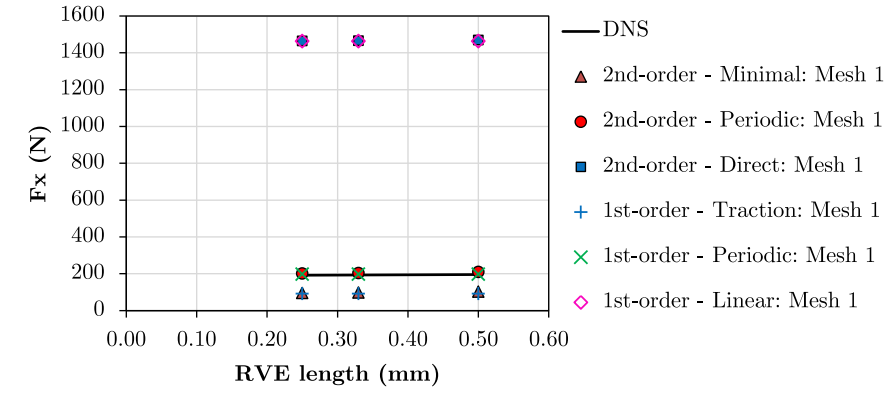

(a) Loading programme associated with tension.

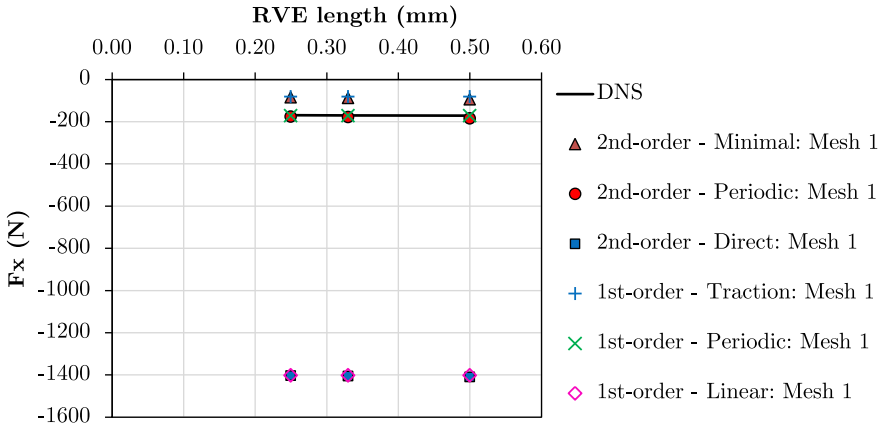

(b) Loading programme associated with compression.

Fig. 10. Size effect study considering the macro-scale mesh 1: RVE length x reaction force (F_x).

Table 4
Size effect study considering the macro-scale mesh 1 for loading programme associated with tension: differences in reaction forces (F_x) for second-order multi-scale models compared to DNS models.

RVE length	F_x (N) and difference compared to DNS model						
(mm)	DNS	Minimal		Periodic		Direct	
l_μ = 0.500 mm	194.89	102.58	47.36%	209.95	7.73%	1469.22	653.88%
l_μ = 0.333 mm	192.88	97.30	49.55%	203.35	5.43%	1465.75	659.94%
l_μ = 0.250 mm	191.89	95.10	50.44%	200.77	4.63%	1464.47	663.19%

Table 5
Size effect study considering the macro-scale mesh 1 for loading programme associated with tension: differences in reaction forces (F_x) for first-order multi-scale models compared to DNS models.

RVE length	F_x (N) and difference compared to DNS model						
(mm)	DNS	Uniform traction		Periodic		Linear	
l_μ = 0.500 mm	194.89	91.57	53.02%	196.69	0.93%	1462.73	650.55%
l_μ = 0.333 mm	192.88	91.57	52.53%	196.69	1.98%	1462.73	658.38%
l_μ = 0.250 mm	191.89	91.57	52.28%	196.69	2.50%	1462.73	662.29%

in Eq. (31), i.e.,

$$\begin{bmatrix} P_{11} \\ P_{21} \\ P_{12} \\ P_{22} \end{bmatrix} = \begin{bmatrix} A_{1111} & A_{1121} & A_{1112} & A_{1122} \\ A_{2111} & A_{2121} & A_{2112} & A_{2122} \\ A_{1211} & A_{1221} & A_{1212} & A_{1222} \\ A_{2211} & A_{2221} & A_{2212} & A_{2222} \end{bmatrix} \begin{bmatrix} F_{11} - 1 \\ F_{21} \\ F_{12} \\ F_{22} - 1 \end{bmatrix}. \tag{32}$$

In this context, the initial results of $\mathbf{A}$ for multi-scale models are presented in matrix representation ($\boldsymbol{A}$) as follows:

(i) linear boundary condition (first-order model) and direct constraint (second-order model):

$$\boldsymbol{A}^{linear}_{1st-order} \approx \boldsymbol{A}^{direct}_{second-order} = \begin{bmatrix} 16045.84 & -11492.74 & -11492.74 & 11722.31 \\ -11492.74 & 14105.26 & 14105.26 & -9740.49 \\ -11492.74 & 14105.26 & 14105.26 & -9740.49 \\ 11722.31 & -9740.49 & -9740.49 & 58206.23 \end{bmatrix} \text{MPa},$$

(ii) periodic boundary condition (first-order model) and periodic constraint (second-order model):

$$\boldsymbol{A}^{periodic}_{1st-order} \approx \boldsymbol{A}^{periodic}_{2nd-order} = \begin{bmatrix} 12418.76 & -11928.96 & -11928.96 & 10715.56 \\ -11928.96 & 12158.33 & 12158.33 & -10949.70 \\ -11928.96 & 12158.33 & 12158.33 & -10949.70 \\ 10715.56 & -10949.70 & -10949.70 & 57206.25 \end{bmatrix} \text{MPa},$$

(iii) uniform traction boundary condition (first-order model) and minimum constraint (second-order model):

$$\boldsymbol{A}^{traction}_{1st-order} \approx \boldsymbol{A}^{minimal}_{2nd-order} = \begin{bmatrix} 3555.25 & -2693.13 & -2693.13 & 2500.95 \\ -2693.13 & 2225.52 & 2225.52 & -2010.42 \\ -2693.13 & 2225.52 & 2225.52 & -2010.42 \\ 2500.95 & -2010.42 & -2010.42 & 48814.20 \end{bmatrix} \text{MPa},$$

where the responses are similar for all RVE lengths. It is also worth mentioning that the initial values for $\boldsymbol{A}$ are the same in tension and

Table 6
Size effect study considering the macro-scale mesh 1 for loading programme associated with compression: differences in reaction forces (F_x) for second-order multi-scale models compared to DNS models.

RVE length	F_x (N) and difference compared to DNS model						
(mm)	DNS	Minimal		Periodic		Direct	
l_μ = 0.500 mm	−171.81	−94.08	45.24%	−185.06	7.71%	−1409.28	720.27%
l_μ = 0.333 mm	−170.31	−87.94	48.36%	−178.30	4.69%	−1405.22	725.09%
l_μ = 0.250 mm	−169.56	−85.32	49.68%	−175.72	3.63%	−1403.73	727.85%

Table 7
Size effect study considering the macro-scale mesh 1 for loading programme associated with compression: differences in reaction forces (F_x) for first-order multi-scale models compared to DNS models.

RVE length	F_x (N) and difference compared to DNS model						
(mm)	DNS	Uniform traction		Periodic		Linear	
l_μ = 0.500 mm	−171.81	−81.22	52.73%	−172.00	0.11%	−1401.71	715.86%
l_μ = 0.333 mm	−170.31	−81.22	52.31%	−172.00	0.99%	−1401.71	723.03%
l_μ = 0.250 mm	−169.56	−81.22	52.10%	−172.00	1.44%	−1401.71	726.66%

compression, and that they are not dependent on the type of multi-scale formulation (first or second-order).

It is noteworthy that all components of $\boldsymbol{A}$ have non-null values, unlike the idealisation of Eq. (31). Specifically, negative values arise for components of $\boldsymbol{A}$ (see values highlighted in pink and light grey) compared to Eq. (31). Such components of $\boldsymbol{A}$ with negative values are associated with coupling mechanisms relating to axial tension/compression and shear. Furthermore, the differences between the pink and light grey components occur due to the geometry of the RVE, since the homogenised material is not isotropic and the stiffness depends on the direction. Therefore, the effect of tension/compression-induced undulation is related to the coupling between tension/compression and shear, quantified by the shaded values in the initial consistent tangent $\mathbf{A}$, which is promoted by the geometry of the new micro-architected material.

Moreover, the maximum vertical displacements are superior for the loading associated with compression when compared to the loading programme associated with tension, except for the linear boundary condition (first-order model) and the direct constraint (second-order model), which result in similar responses. In order to explain this difference, Fig. 13 shows the evolution of $\mathbf{A}$ for multi-scale models based on second-order computational homogenisation considering the integration point I_A at macro-scale mesh 1 (see Fig. 9(a)). In addition, Fig. 14 displays the particular case of the A_{2111} component that relates P_{21} with F_{11}, i.e., the coupling effect between shear and tension/compression. It is possible to observe that the evolution of the responses is different for tension and compression, which contributes to the difference in the maximum vertical macroscopic displacements. In particular, the differences in the evolution of $\mathbf{A}$, considering compression and tension, are more pronounced for periodic and minimal constraint, in which a stronger coupling occurs for the compression loading programme. Such observations justify the differences in the maximum displacements observed in periodic and minimal constraint models when comparing tension and compression. Such a difference is not observed for the direct constraint since it is the most restrictive boundary condition. Furthermore, it must be highlighted that only finite strain formulations like those considered here are able to capture these asymmetries due to non-linear geometrical effects. Finally, it is worth mentioning that the conclusions are analogous to multi-scale models based on first-order homogenisation.

3.1.4. Symmetry class of the homogenised material properties

It is also relevant to explore the symmetry class related to the material properties of the new mechanical metamaterial with tension/compression-induced undulation. In this case, three-dimensional simulations are employed to verify more components of the homogenised elastic constitutive tensor associated, unravelling other possible couplings. In this context, an analogous three-dimensional unit cell (see Fig. 15) was simulated to obtain the initial consistent tangent $\mathbf{A}$ that is equivalent to the homogenised elastic constitutive tensor.

For three-dimensional analysis, the constitutive relationship between $\boldsymbol{P}$ and $\boldsymbol{F}$, taking into account $\mathbf{A}$, can be expressed in matrix form as in Eq. (33).

Due to the conditions of major and minor symmetries at the undeformed configuration, an anisotropic material exhibits 21 independent elastic constants. Thus, $\mathbf{A}$ can be rewritten in simplified matrix form as

$$\boldsymbol{A} = \begin{bmatrix} A_{1111} & A_{1122} & A_{1133} & A_{1123} & A_{1131} & A_{1112} \\ A_{2211} & A_{2222} & A_{2233} & A_{2223} & A_{2231} & A_{2212} \\ A_{3311} & A_{3322} & A_{3333} & A_{3323} & A_{3331} & A_{3312} \\ A_{2311} & A_{2322} & A_{2333} & A_{2323} & A_{2331} & A_{1312} \\ A_{3111} & A_{3122} & A_{3133} & A_{3123} & A_{3131} & A_{3112} \\ A_{1211} & A_{1222} & A_{1233} & A_{1223} & A_{1231} & A_{1212} \end{bmatrix}, \tag{34a}$$

where the 6×6 matrix is symmetric due to major symmetry.

For example, considering Eq. (33), the initial consistent tangent for first- and second-order periodic multi-scale models is given in Eq. (34b), where negative components with shear–normal coupling (pink box) and shear–shear coupling (light grey box) can be observed.

It is worth mentioning that material symmetry refers to how constitutive properties vary with respect to direction in a fixed material point. In particular, the new metamaterial is called monoclinic with one plane of material symmetry (in this case, X_3 direction). Therefore, the metamaterial has 13 independent elastic constants.

3.2. Numerical example 2: two-dimensional architected material under bending

The main goal of this numerical experiment is to show the capacity of second-order homogenisation to deal with size effects of architected materials under bending through two-dimensional numerical simulations. The elastic properties for the architected material are $E = 100$ MPa and $\nu = 0.3$. Moreover, the assumption of plane strain is adopted for the two-dimensional structure.

3.2.1. DNS models

The geometry for the periodic unit cells of the architected material is indicated in Fig. 16. Information about all DNS models and the discretisation is provided in Table 8. It is important to note that the material volume fraction remains invariant across all DNS models. The DNS models are created as a periodic array from the unit cell, where different cell sizes are defined. For illustration purposes, Fig. 17 shows three coarser DNS models. Regarding the Dirichlet boundary conditions, the left side of the structure is fixed, i.e., $u_{0x} = u_{0y} = 0.0$. Concerning the Neumann boundary conditions, a uniformly distributed vertical load t_{0y} is applied on the top side of the structure. Specifically, the loading programme $t_{0y} = -5.0 \times 10^{-5}$ N/mm is imposed in 10

$$\begin{bmatrix} P_{11} \\ P_{21} \\ P_{31} \\ P_{12} \\ P_{22} \\ P_{32} \\ P_{13} \\ P_{23} \\ P_{33} \end{bmatrix} = \begin{bmatrix} A_{1111} & A_{1121} & A_{1131} & A_{1112} & A_{1122} & A_{1132} & A_{1113} & A_{1123} & A_{1133} \\ A_{2111} & A_{2121} & A_{2131} & A_{2112} & A_{2122} & A_{2132} & A_{2113} & A_{2123} & A_{2133} \\ A_{3111} & A_{3121} & A_{3131} & A_{3112} & A_{3122} & A_{3132} & A_{3113} & A_{3123} & A_{3133} \\ A_{1211} & A_{1221} & A_{1231} & A_{1212} & A_{1222} & A_{1232} & A_{1213} & A_{1223} & A_{1233} \\ A_{2211} & A_{2221} & A_{2231} & A_{2212} & A_{2222} & A_{2232} & A_{2213} & A_{2223} & A_{2233} \\ A_{3211} & A_{3221} & A_{3231} & A_{3212} & A_{3222} & A_{3232} & A_{3213} & A_{3223} & A_{3233} \\ A_{1311} & A_{1321} & A_{1331} & A_{1312} & A_{1322} & A_{1332} & A_{1313} & A_{1323} & A_{1333} \\ A_{2311} & A_{2321} & A_{2331} & A_{2312} & A_{2322} & A_{2332} & A_{2313} & A_{2323} & A_{2333} \\ A_{3311} & A_{3321} & A_{3331} & A_{3312} & A_{3322} & A_{3332} & A_{3313} & A_{3323} & A_{3333} \end{bmatrix} \begin{bmatrix} F_{11} - 1 \\ F_{21} \\ F_{31} \\ F_{12} \\ F_{22} - 1 \\ F_{32} \\ F_{13} \\ F_{23} \\ F_{33} - 1 \end{bmatrix}. \tag{33}$$

$$\boldsymbol{A}^{periodic}_{1st-order} = \boldsymbol{A}^{periodic}_{2nd-order} = \begin{bmatrix} 12473.61 & 10763.24 & 6971.06 & 0.00 & 0.00 & -11957.20 \\ 10763.24 & 57342.19 & 20431.63 & 0.00 & 0.00 & -10976.77 \\ 6971.06 & 20431.63 & 83820.80 & 0.00 & 0.00 & -6880.19 \\ 0.00 & 0.00 & 0.00 & 22287.91 & -6891.89 & 0.00 \\ 0.00 & 0.00 & 0.00 & -6891.89 & 9241.15 & 0.00 \\ -11957.20 & -10976.77 & -6880.19 & 0.00 & 0.00 & 12186.84 \end{bmatrix} \text{MPa}, \tag{34b}$$

Table 8
Mesh of DNS models.

DNS	Elements (Q8)	Nodes
Model 1 - Size 1 (l_μ = 1.000 mm)	3800	14 960
Model 2 - Size 2 (l_μ = 0.500 mm)	15 200	57 819
Model 3 - Size 3 (l_μ = 0.250 mm)	60 800	227 237
Model 4 - Size 4 (l_μ = 0.167 mm)	136 800	508 255
Model 5 - Size 5 (l_μ = 0.125 mm)	243 200	900 873
Model 6 - Size 6 (l_μ = 0.100 mm)	380 000	1 405 091

equally spaced increments. Moreover, the distribution of the applied load provides a linear shear force and a quadratic bending moment along the length (L_x) of the structure.

A comparison of the vertical displacements for three DNS models is shown in Fig. 18. It is clear that the length of the unit cell plays an important role in the deformable behaviour of the structure. In summary, decreasing the unit cell size increases the maximum displacements of DNS models, i.e., the structure becomes more flexible. Consequently, DNS model 1 is the stiffest and DNS model 3 is the most flexible. Furthermore, the deformed configuration of DNS model 2 is closer to the response observed for DNS model 3. Thus, the size effects cannot be neglected in the structure and higher-order continuum theories can be necessary for modelling this type of architected material.

3.2.2. Multi-scale simulations

This bending problem is also solved using multi-scale FE^2 models, with both first and second-order homogenisation approaches. Different classes of boundary conditions are also considered, similar to the analysis performed in Section 3.1.2.

The RVE geometry and mesh were previously presented in Fig. 16. Regarding the macro-scale, the geometry and boundary conditions are illustrated in Fig. 19. Moreover, mixed quadrilateral finite elements (Q8F4L1) with 4 integration points are defined for macro-scale (Rodrigues Lopes and Andrade Pires, 2022d). To perform a numerical convergence analysis, three meshes (see Fig. 20) were employed to discretise the macro-scale domain, and the simulations have been performed with an RVE length l_μ = 1.000 mm. The obtained maximum vertical displacements are presented in Table 9, where it is observed that the maximum values are similar for all meshes due to small relative differences. Consequently, mesh 1 is adopted for investigating the architected material, from a multi-scale perspective.

In order to investigate the microstructural size effect, six values were considered for the RVE length: l_μ = 1.000 mm (size 1), l_μ = 0.500 mm (size 2), l_μ = 0.250 mm (size 3), l_μ = 0.167 mm (size 4), l_μ = 0.125 mm (size 5) and l_μ = 0.100 mm (size 6). The results for the maximum vertical displacement associated with each characteristic length are shown in Fig. 21, where the values obtained with the multi-scale models, both first- and second-order homogenisation, are represented along with the corresponding DNS results. Tables 10 and 11 show the differences (in module) of multi-scale models compared to DNS models. In addition, Figs. 22 and 23 show the results of the vertical displacements of the deformed structures (l_μ = 1.000 mm) for the first- and second-order homogenisation strategies, respectively.

In general, second-order multi-scale models (minimal, periodic and direct constraints) have similar results. An analogous conclusion is observed for first-order multi-scale models (uniform traction, periodic and linear boundary conditions). Moreover, since the size effect is significant in this structure, the first-order (so-called classical) multi-scale computational homogenisation scheme loses accuracy. It must be highlighted that the response obtained with first-order homogenisation is independent of the RVE length, and significant differences are observed for larger RVEs. On the other hand, second-order multi-scale computational homogenisation models capture the trend observed in the DNS models, with an increase of the maximum displacements for a reduction in the RVE size. It is worth noting that the responses are close for smaller characteristic lengths of RVE. Therefore, second-order homogenisation is needed to better predict the macroscopic behaviour of the architected material, in particular, to capture the underlying size effects.

3.3. Numerical example 3: three-dimensional architected material under bending

This example aims to investigate an architected material under bending through three-dimensional numerical simulations. The material properties for the matrix are E = 100 MPa and ν = 0.3.

3.3.1. DNS models

In this case, the architected material under study consists of periodic cellular materials formed by the unit cell shown in Fig. 24. Fig. 25 presents the DNS models that represent the architected structures. Since the structures are composed of a periodic arrangement of unit cells, the volume fraction of the material is constant in all DNS models. The left side of the structures is fixed, i.e., the following Dirichlet boundary conditions are prescribed: $u_{0x} = u_{0y} = u_{0z} = 0$. The loading programme consists of a vertical tangential distributed load $t_{0y} = -1.0 \times 10^{-3}$ N/mm^2 imposed on the right side of the structure considering 10 increments (see detail in Fig. 26). With respect to internal forces, the distribution of the applied load indicates a constant shear force and a

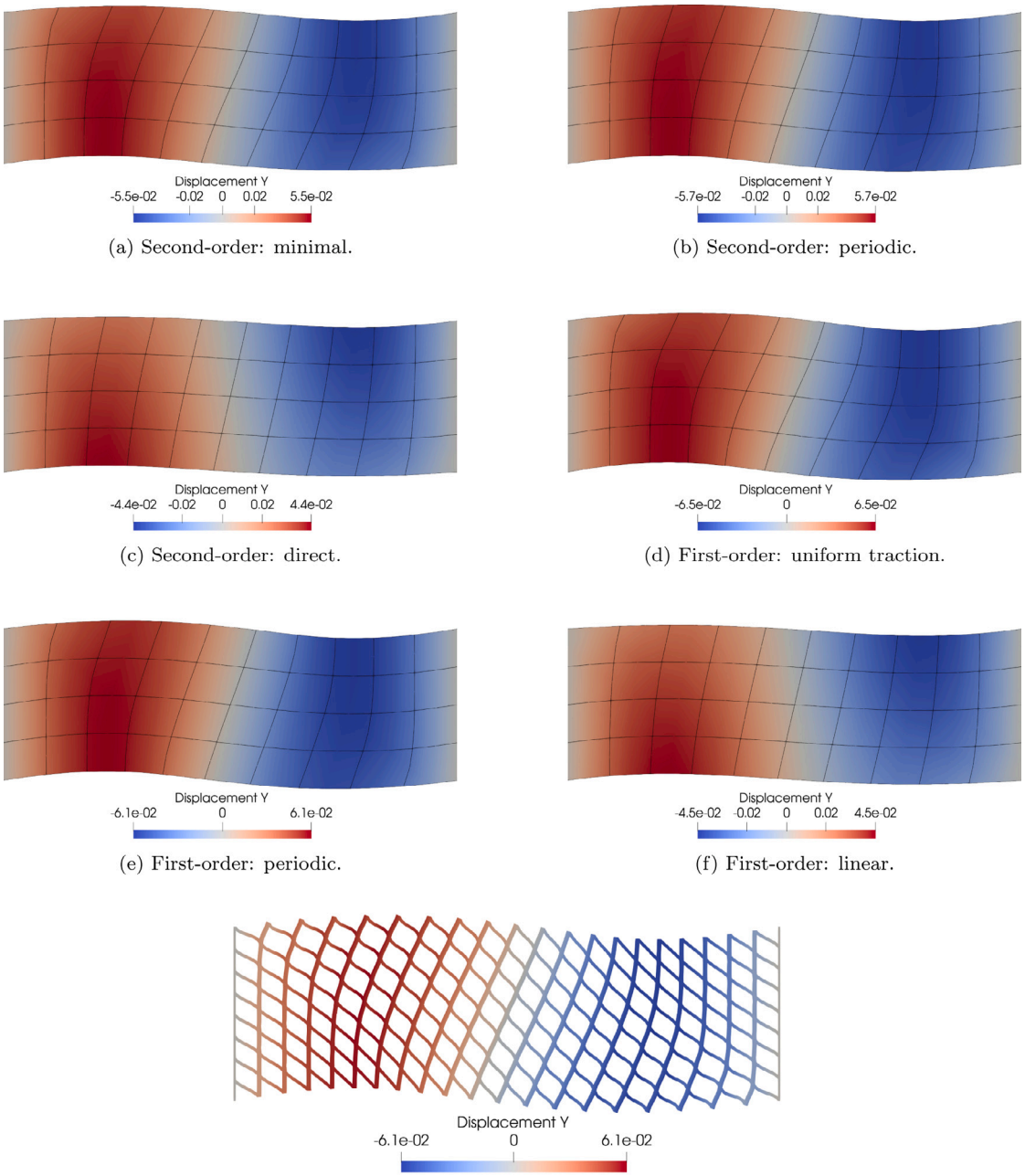

(a) Second-order: minimal.

(b) Second-order: periodic.

(c) Second-order: direct.

(d) First-order: uniform traction.

(e) First-order: periodic.

(f) First-order: linear.

(g) DNS model 1 (20x8 unit cells).

Fig. 11. Vertical displacements in mm (scale factor = 4) for first- and second-order models compared to DNS model considering the RVE length 1, i.e., l_μ = 0.500 mm, and the loading programme related to axial tension.

Table 9
Mesh study considering the maximum vertical displacement U_y (mm) on the right side of the structure for RVE size 1 (l_μ = 1.000 mm).

	Vertical displacement U_y (mm)				
	Mesh 1	Mesh 2	Mesh 3	Differences in module	
Multi-scale models	(1)	(2)	(3)	(2) to (1)	(3) to (2)
2nd-order: Minimal	−0.3956	−0.3923	−0.3906	0.83%	0.45%
2nd-order: Periodic	−0.3932	−0.3899	−0.3883	0.84%	0.40%
2nd-order: Direct	−0.3911	−0.3879	−0.3863	0.82%	0.43%
1st-order: Uniform traction	−1.4063	−1.4076	−1.4077	0.09%	0.01%
1st-order: Periodic	−1.3098	−1.3101	−1.3102	0.02%	0.01%
1st-order: Linear	−1.3052	−1.3056	−1.3057	0.03%	0.01%

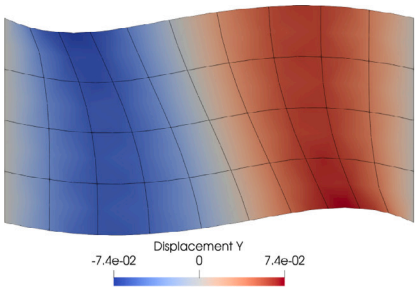

(a) Second-order: Minimal.

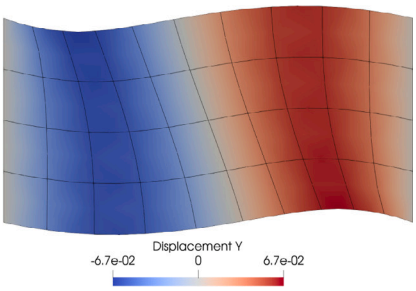

(b) Second-order: Periodic.

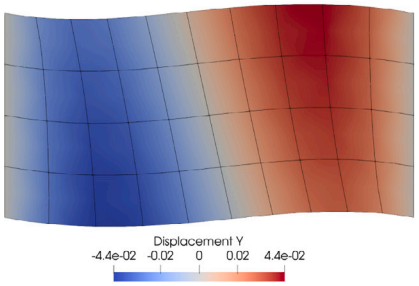

(c) Second-order: Direct.

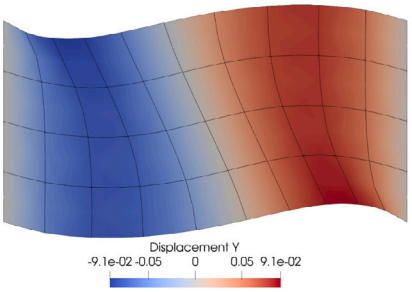

(d) First-order: Uniform traction.

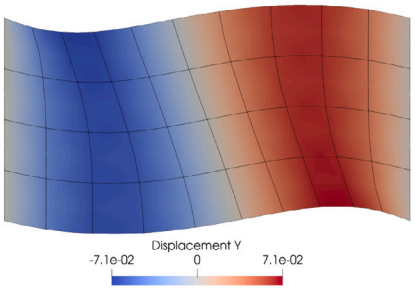

(e) First-order: Periodic.

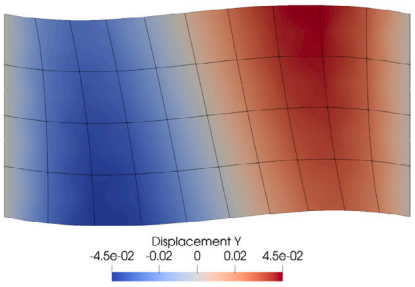

(f) First-order: Linear.

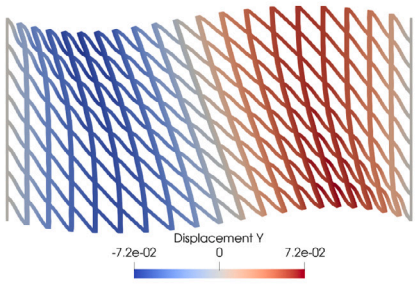

(g) DNS model 1 (20x8 unit cells).

Fig. 12. Vertical displacements in mm (scale factor = 4) for first- and second-order models compared to DNS model considering the RVE length 1, i.e., l_μ = 0.500 mm, and the loading programme related to axial compression.

linear bending moment along the length (L_x) of the structure. Meshes data for the DNS models are shown in Table 12, where the 20-node hexahedron element (H20) and 8 integration points were defined to create the structured meshes. Since a large number of unit cells results in a significant increase in elements and degrees of freedom of the mesh, more refined DNS models were limited by the available memory requirements of the computer used in the numerical simulations. This limitation regarding memory requirements highlights a drawback of more refined DNS models, whose simulation may become impractical.

Fig. 27 presents a comparison of the vertical displacements for the DNS models. DNS model 1 is the structure with the most stiffness, while DNS model 3 is the most flexible. The DNS 2 model presents an intermediate response, being closer to the DNS 3 model. In this manner, the architected structure has the so-called size dependence related to material microstructure. Therefore, the generalised continuum mechanics can be more suitable for modelling this numerical example.

3.3.2. *Multi-scale simulations*

In the context of multi-scale numerical simulations based on first and second-order computational homogenisation, the results are shown only for periodic boundary conditions due to the better results when compared with the DNS models. Regarding the coupled multi-scale simulations, geometry and mesh parameters must be defined for the macro and micro-scales. The RVE data are shown in Fig. 24, including

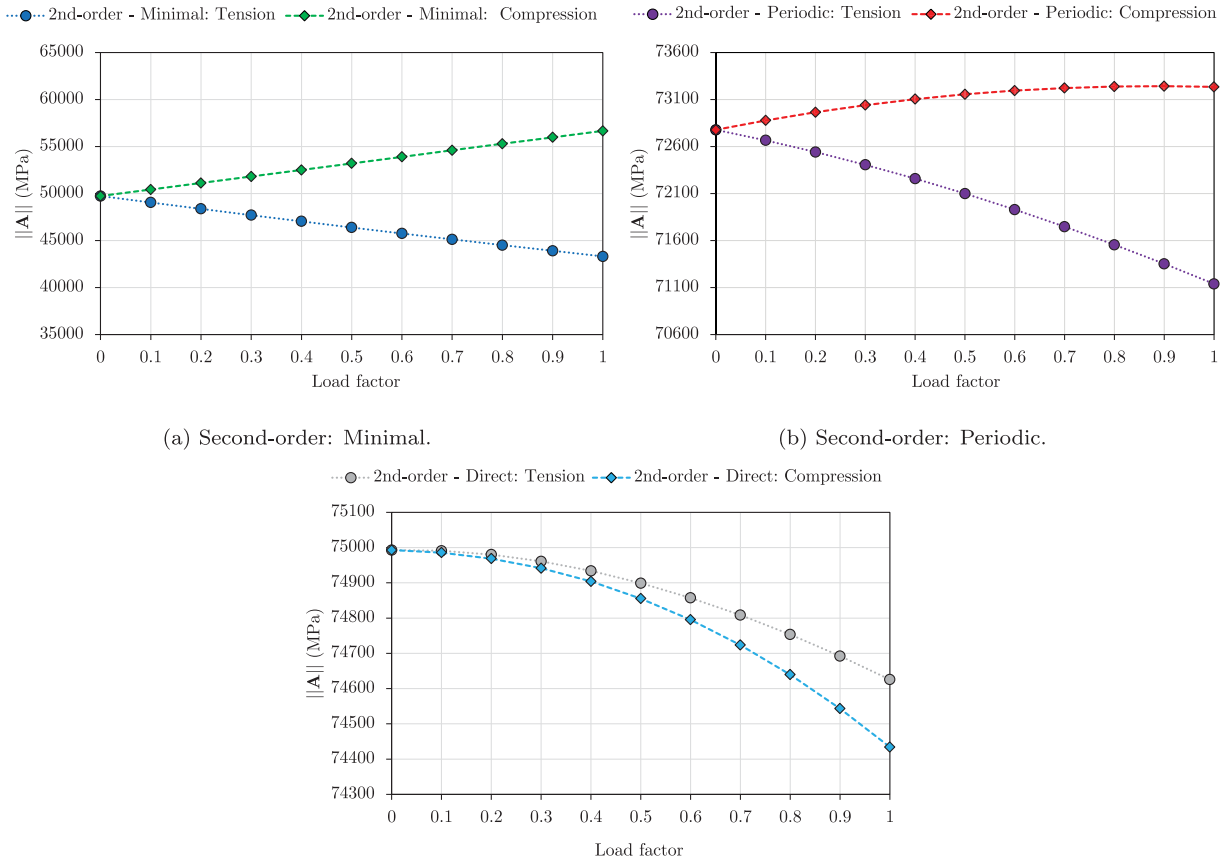

(a) Second-order: Minimal.

(b) Second-order: Periodic.

(c) Second-order: Direct.

Fig. 13. Norm of **A** required for multi-scale modelling based on second-order homogenisation: comparison between compression and tension loading programmes.

Table 10
Maximum vertical displacement on the right side of the structure (U_y) for all second-order multiscale models, including differences in comparison with DNS models.

RVE length	U_y (mm) and differences compared to DNS model						
(mm)	DNS	Minimal		Periodic		Direct	
l_μ = 1.000	−0.545	−0.396	27.46%	−0.393	27.92%	−0.391	28.29%
l_μ = 0.500	−0.970	−0.825	14.92%	−0.820	15.46%	−0.817	15.72%
l_μ = 0.250	−1.206	−1.146	4.98%	−1.138	5.64%	−1.135	5.87%
l_μ = 0.167	−1.262	−1.235	2.16%	−1.226	2.86%	−1.223	3.08%
l_μ = 0.125	−1.284	−1.270	1.06%	−1.261	1.77%	−1.258	1.99%
l_μ = 0.100	−1.294	−1.287	0.52%	−1.277	1.24%	−1.275	1.47%

Table 11
Maximum vertical displacement on the right side of the structure (U_y) for all first-order multiscale models, including differences compared to DNS models.

RVE length	U_y (mm) and differences compared to DNS model						
(mm)	DNS	Uniform traction		Periodic		Linear	
l_μ = 1.000	−0.545	−1.406	157.84%	−1.310	140.15%	−1.305	139.30%
l_μ = 0.500	−0.970	−1.406	45.02%	−1.310	35.07%	−1.305	34.59%
l_μ = 0.250	−1.206	−1.406	16.65%	−1.310	8.65%	−1.305	8.27%
l_μ = 0.167	−1.262	−1.406	11.40%	−1.310	3.76%	−1.305	3.39%
l_μ = 0.125	−1.284	−1.406	9.57%	−1.310	2.05%	−1.305	1.69%
l_μ = 0.100	−1.294	−1.406	8.72%	−1.310	1.26%	−1.305	0.90%

the mesh modelled with hexahedral elements (H20) and 8 integration points. Fig. 28 illustrates the geometry and boundary conditions for the macro-scale. Mixed hexahedral elements with 20 nodes (H20F8L1) and 8 integration points are employed to discretise the macro-scale (Rodrigues Lopes and Andrade Pires, 2022b). A mesh refinement study was

Table 12
Mesh of DNS models.

DNS	Elements (H20)	Nodes
Model 1 - Size 1 (l_μ = 1.000 mm)	9000	59 316
Model 2 - Size 2 (l_μ = 0.500 mm)	72 000	426 181
Model 3 - Size 3 (l_μ = 0.333 mm)	243 000	1 385 596

performed for the macro-scale, in which two meshes were investigated (see Fig. 29) for l_μ = 1.000 mm. As shown in Fig. 30, the mesh convergence study was carried out, taking into account the maximum vertical displacements of the structure. The responses are very close for both meshes defined at the macro-scale, i.e., the result of mesh 1 is in close agreement with the result of mesh 2. Thus, mesh 1 is sufficient to compute the numerical simulations.

Fig. 31 shows the results of the size effects study for the architected structures, in which multi-scale simulations based on first- and second-order computational homogenisation with the periodic constraint are confronted with DNS models. In this case, seven RVE lengths were considered for the multi-scale simulations: l_μ = 1.000 mm (size 1), l_μ = 0.500 mm (size 2), l_μ = 0.333 mm (size 3), l_μ = 0.250 mm (size 4), l_μ = 0.167 mm (size 5), l_μ = 0.125 mm (size 6) and l_μ = 0.100 mm (size 7). Note that multi-scale simulations allow us to consider smaller RVE lengths with similar computational cost and memory requirements, which is an advantage compared to DNS models that were unfeasible due to the limited memory requirements of the processing computer. The vertical displacements for first- and second-order multi-scale periodic boundary conditions are presented in Figs. 32 and 33, respectively. The second-order homogenisation captures the increase in the maximum vertical displacement with the reduction

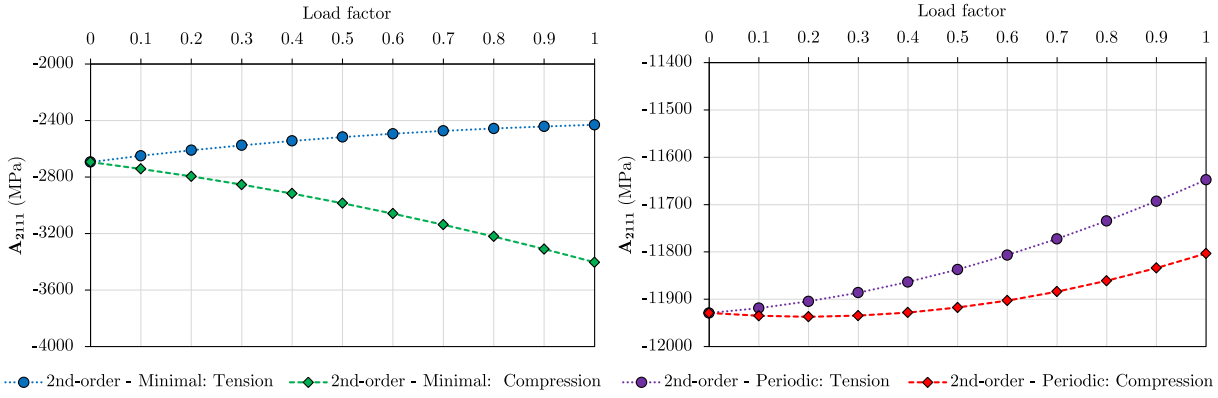

(a) Second-order: Minimal.

(b) Second-order: Periodic.

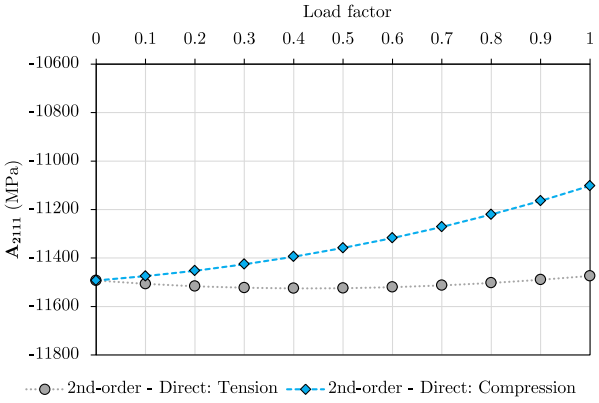

(c) Second-order: Direct.

Fig. 14. Results for A_{2111} component with coupling between P_{21} and F_{11} considering the multi-scale modelling based on second-order homogenisation: comparison between compression and tension loading programmes.

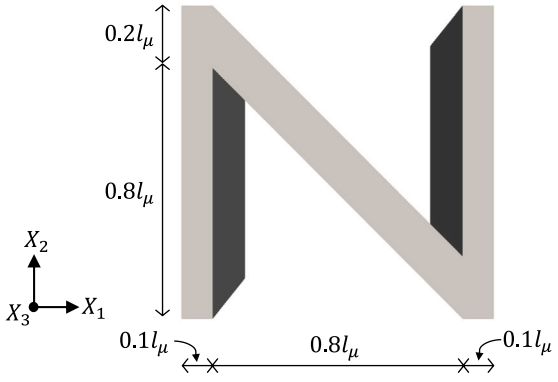

(a) Geometry.

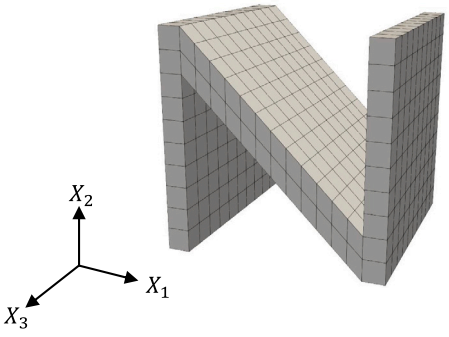

(b) Mesh: 440 elements (20-node hexahedron or H20) and 2937 nodes.

Fig. 15. Three-dimensional unit cell or RVE.

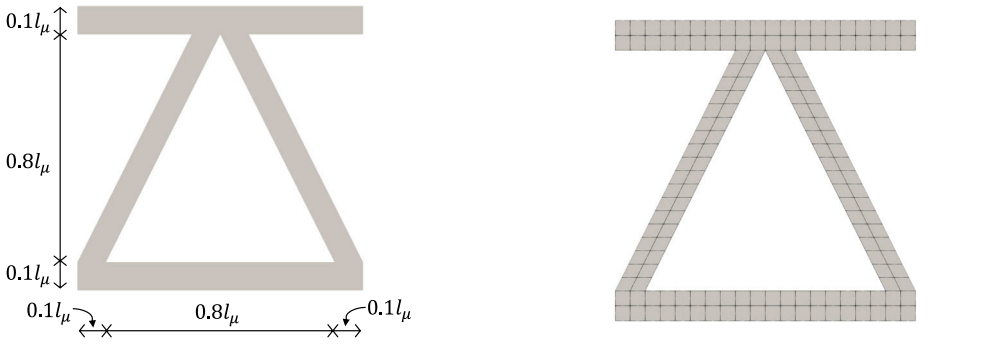

(a) Geometry.

(b) Mesh: 152 elements (Q8) and 608 nodes.

Fig. 16. Unit cell and RVE.

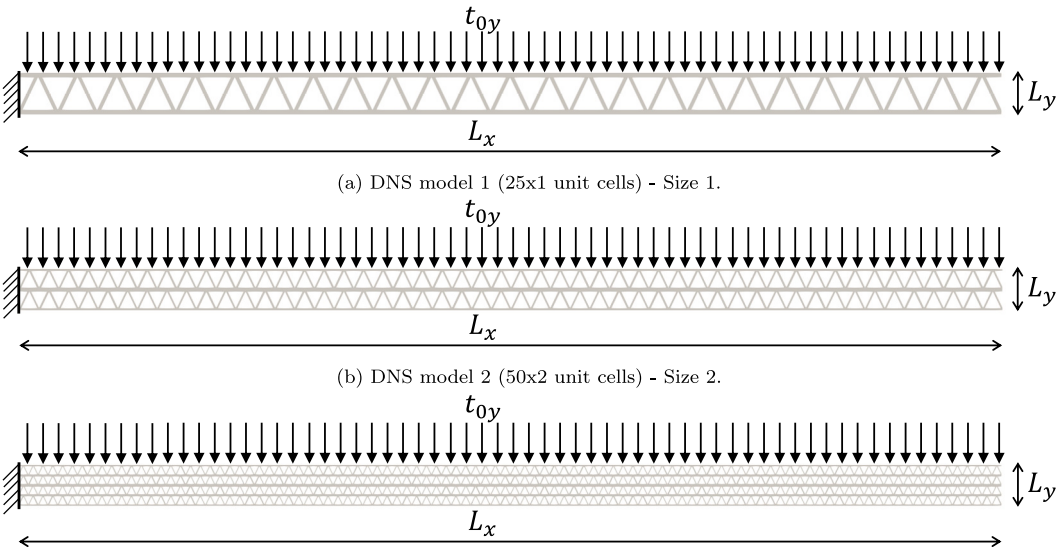

(a) DNS model 1 (25x1 unit cells) - Size 1.

(b) DNS model 2 (50x2 unit cells) - Size 2.

(c) DNS model 3 (100x4 unit cells) - Size 3.

Fig. 17. Geometry of three DNS models (L_x = 25 mm and L_y = 1 mm).

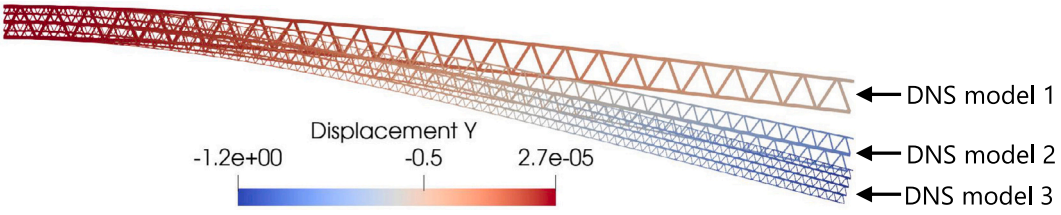

Fig. 18. Vertical displacement results for three DNS models (scale factor = 4).

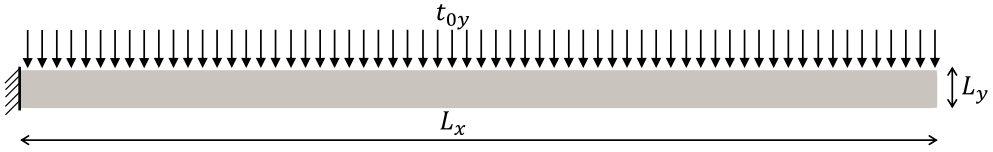

Fig. 19. Geometry and boundary conditions.

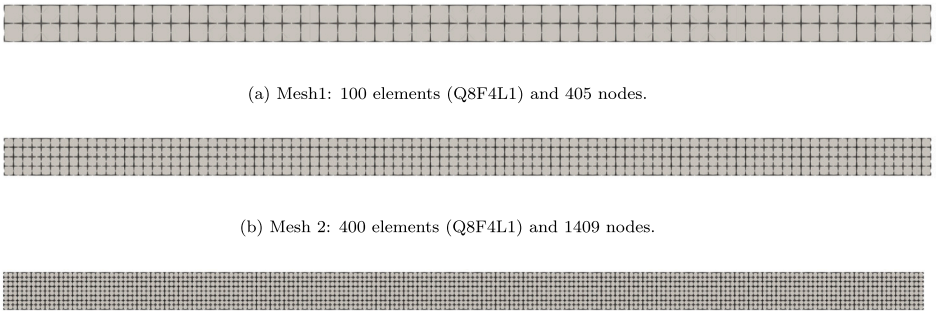

(a) Mesh1: 100 elements (Q8F4L1) and 405 nodes.

(b) Mesh 2: 400 elements (Q8F4L1) and 1409 nodes.

(c) Mesh 3: 1600 elements (Q8F4L1) and 5217 nodes.

Fig. 20. Macro-scale meshes.

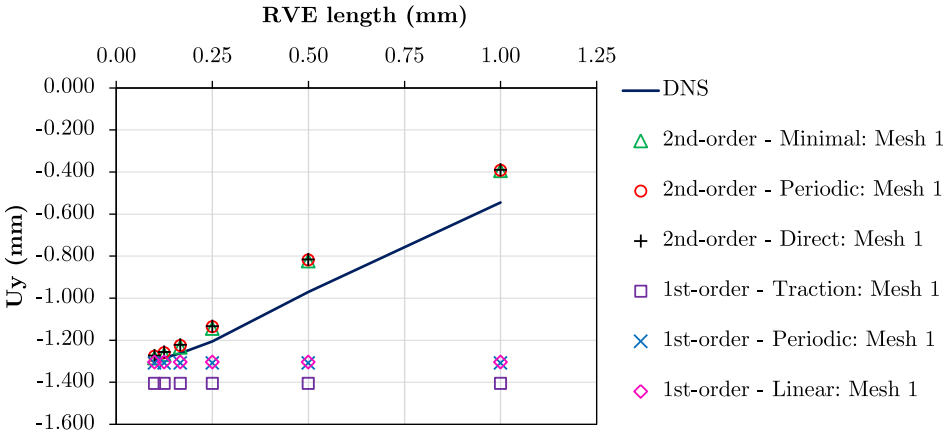

Fig. 21. RVE length x maximum vertical displacement U_y (mm) on the right side of the structure for macro-mesh 1.

of the RVE length. As observed in the DNS models, the periodic second-order multi-scale model associated with RVE size 2 (i.e., l_μ = 0.500 mm) provides a deformed response close to the RVE size 3 (i.e., l_μ = 0.333 mm). Therefore, the qualitative results of the second-order approach adhere to the DNS models. The quantitative differences between the second-order approach and DNS models can be associated with higher-order terms not covered in the second-order strategy. Furthermore, second-order effects were not adequately captured by first-order homogenisation, where significant differences are observed in comparison to DNS models.

3.4. Numerical example 4: three-dimensional metamaterial with compression-induced twisting

The purpose of this example is to simulate three-dimensional metamaterials with twisting behaviour when subjected to compression loading, i.e., compression-induced twisting. Concerning the elastic properties of the matrix, the metamaterial is modelled with E = 210 GPa and ν = 0.3.

3.4.1. DNS models

The morphology for the unit cells of the DNS models is shown in Fig. 35, where the non-symmetric geometry is intentionally designed to provide compression–torsion coupling. The numerical simulations are performed considering the 8-node hexahedron solid element (H8) with 8 integration points. The unit cell mesh is composed of 1216 elements (H8) and 2700 nodes. In order to assess the size effect, four DNS models were simulated (see Fig. 35). Note that the material volume fraction remains constant across all DNS models. The bottom side of the structure has the nodes fixed in the 3 directions, i.e., $u_{0x} = u_{0y} = u_{0z} = 0.0$. With respect to the top side of the structure, a compressive displacement of $u_{0y} = -0.1$ mm is prescribed in the vertical direction, considering 20 increments. Table 13 indicates the mesh data for each DNS model. Furthermore, more refined DNS models were not added due to the limitation of available memory requirements of the computer used for the numerical simulations.

Table 13
Mesh of DNS models.

DNS	Elements (H8)	Nodes
Model 1 - Size 1 (l_μ = 0.500 mm)	29 184	56 235
Model 2 - Size 2 (l_μ = 0.333 mm)	98 496	185 104
Model 3 - Size 3 (l_μ = 0.250 mm)	233 472	433 293
Model 4 - Size 4 (l_μ = 0.167 mm)	787 968	1 444 087

Fig. 36 presents the front view of the deformed DNS models after imposing the load programme. Thus, the deformed structures show the conversion of axial compression into torsion, i.e., a behaviour with compression-induced twisting. Furthermore, the size effect is also clear in the metamaterial, where the reduction of the rotation angle due to the decrease in the unit cell length is observed for DNS models. Fig. 37, with the top view of the deformed DNS models, also helps to visualise the reduction in rotation due to the decrease in the RVE length.

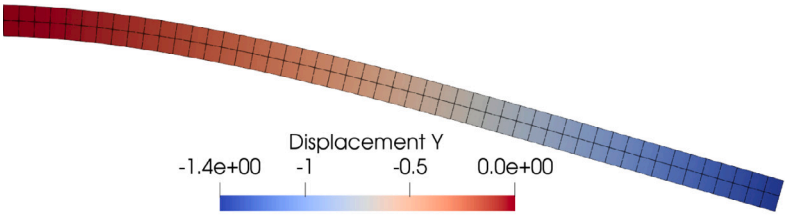

(a) First-order: Uniform traction.

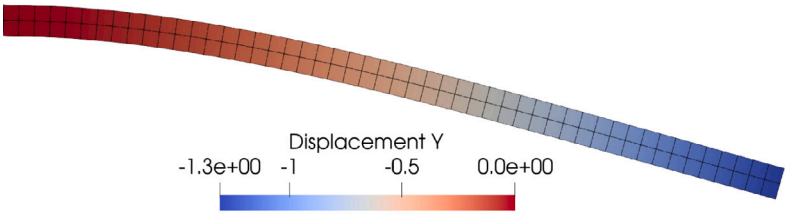

(b) First-order: Periodic.

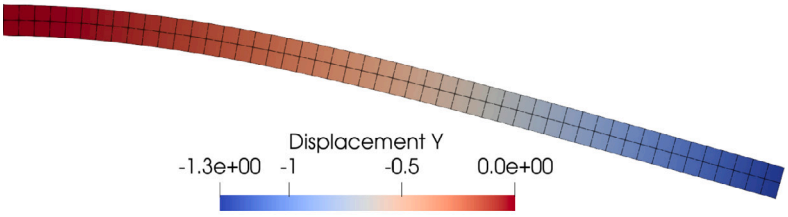

(c) First-order: Linear.

Fig. 22. Vertical displacements (mm) for first-order multi-scale models: all RVE sizes (scale factor = 4).

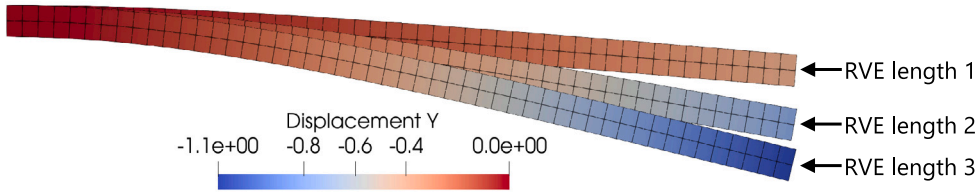

(a) Second-order: Minimal.

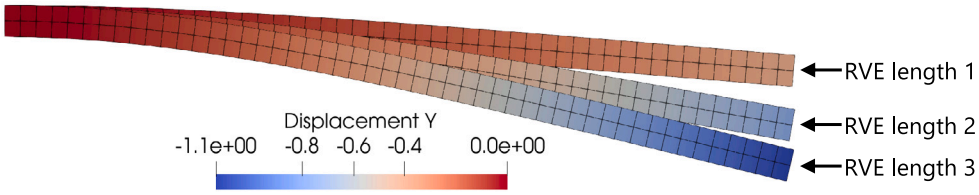

(b) Second-order: Periodic.

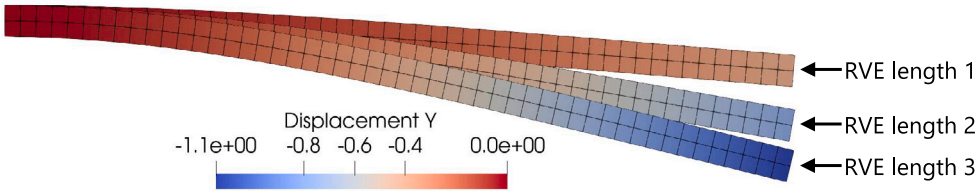

(c) Second-order: Direct.

Fig. 23. Vertical displacements (mm) for second-order multi-scale models: Size 1, 2 and 3 (scale factor = 4).

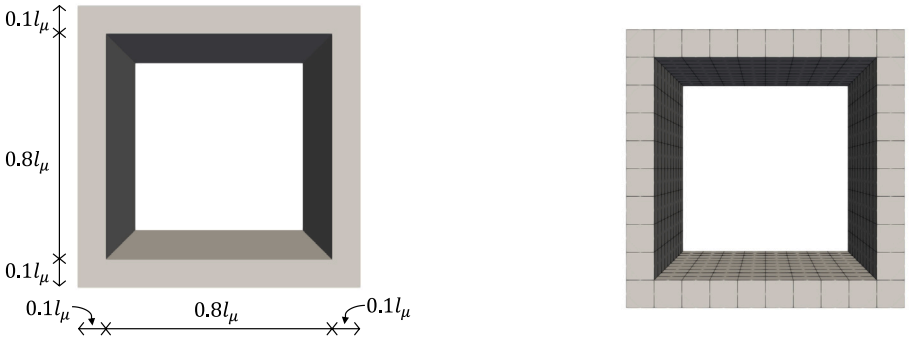

(a) Geometry.

(b) Mesh: 360 elements (H20) and 2700 nodes.

Fig. 24. Unit cell and RVE.

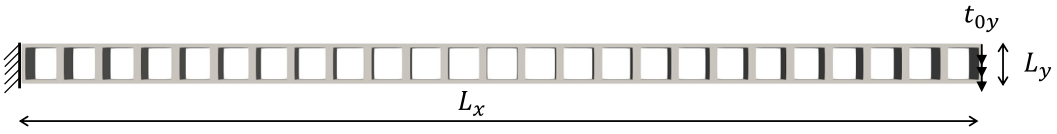

(a) DNS model 1 (25x1x1 unit cells): Size 1.

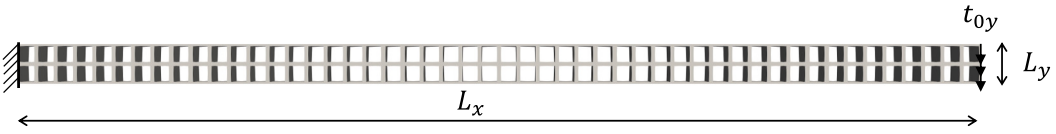

(b) DNS model 2 (50x2x2 unit cells): Size 2.

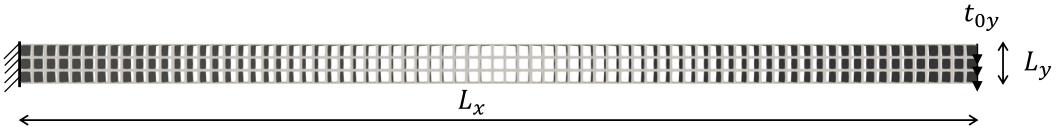

(c) DNS model 3 (75x3x3 unit cells): Size 3.

Fig. 25. Geometry of the DNS models (L_x = 25 mm and $L_y = L_z$ = 1 mm).

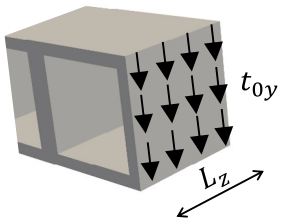

(a) DNS model 1 (25x1x1 unit cells).

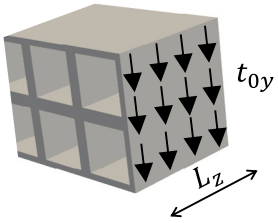

(b) DNS model 2 (50x2x2 unit cells).

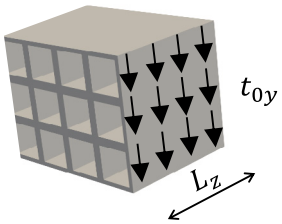

(c) DNS model 3 (75x3x3 unit cells).

Fig. 26. Detail of distributed vertical loading (t_{oy}) applied on the right side of DNS models.

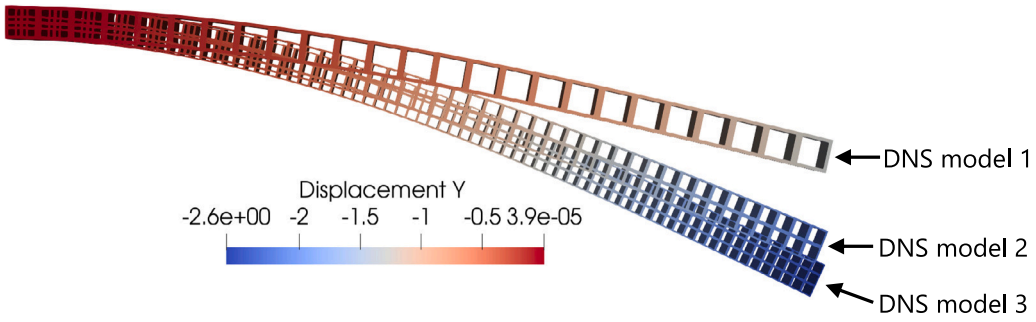

Fig. 27. Comparison of vertical displacements (mm) for DNS models (scale factor = 3).

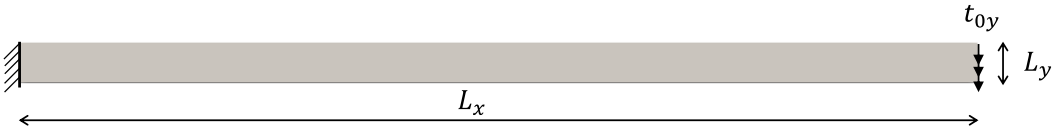

(a) Macro-scale.

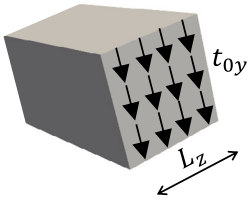

(b) Detail of distributed vertical loading (t_{oy}) applied on the right side of the macro-scale.

Fig. 28. Geometry and boundary conditions for macro-scale (L_x = 25 mm and $L_y = L_z$ = 1 mm).

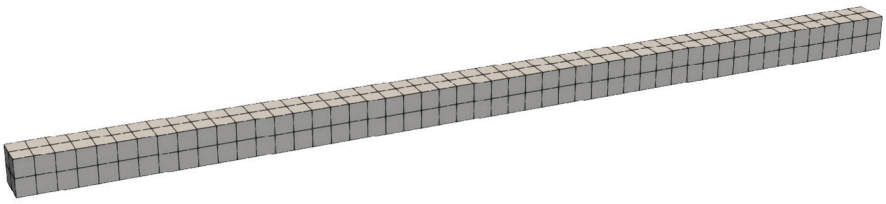

(a) Mesh 1: 200 elements (H20F8L1) and 1521 nodes.

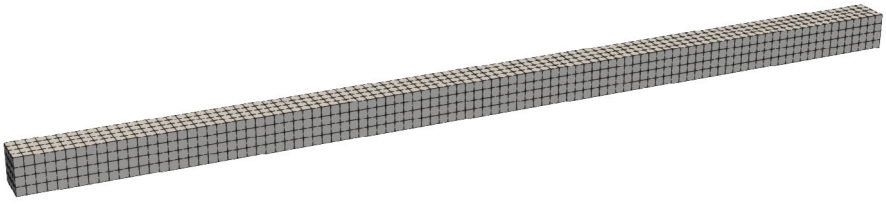

(b) Mesh 2: 1600 elements (H20F8L1) and 9065 nodes.

Fig. 29. Macro-scale meshes.

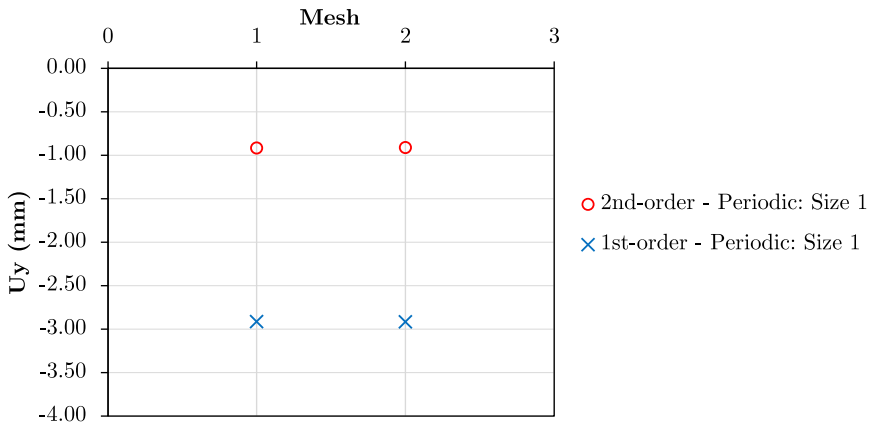

Fig. 30. Mesh study for RVE size 1 (l_μ = 1.000 mm) taking into account the maximum vertical displacement U_y (mm) on the right side of the structure: second-order periodic constraint (2nd-order — Periodic: Size 1) and first-order periodic boundary condition (1st-order — Periodic: Size 1).

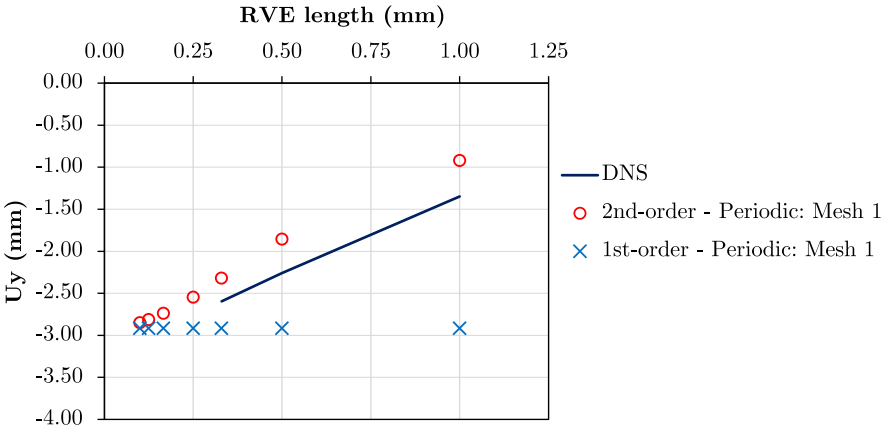

Fig. 31. RVE length x maximum vertical displacement U_y (mm) on the right side of the structure: second-order periodic constraint with macro-scale mesh 1 (2nd-order — Periodic: Mesh 1) and first-order periodic boundary condition with macro-scale mesh 1 (1st-order — Periodic: Mesh 1).

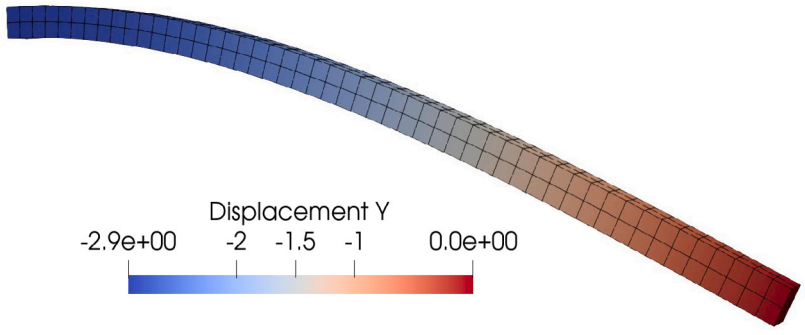

Fig. 32. Vertical displacements (mm) for first-order multi-scale periodic boundary condition: Size 1, 2 and 3 (scale factor = 3).

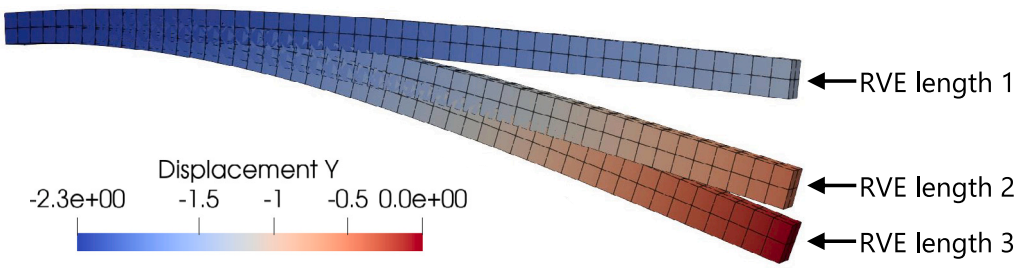

Fig. 33. Vertical displacements (mm) for second-order multi-scale periodic constraint: all RVE sizes (scale factor = 3).

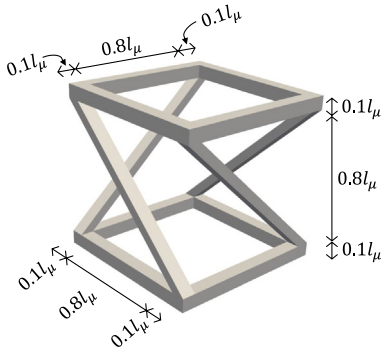

(a) Geometry.

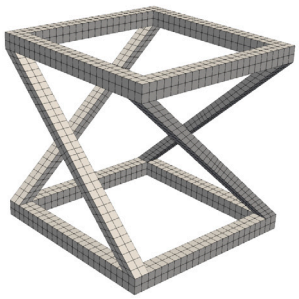

(b) Mesh: 1216 elements (H8) and 2700 nodes.

Fig. 34. Unit cell and RVE.

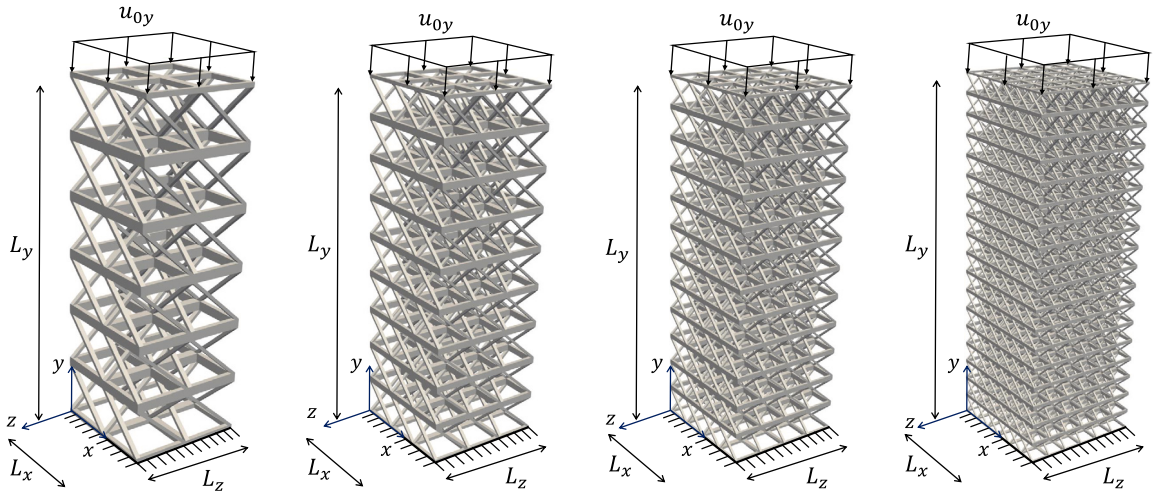

(a) DNS model 1 (2x6x2 unit cells): Size 1.

(b) DNS model 2 (4x12x4 unit cells): Size 2.

(c) DNS model 3 (4x12x4 unit cells): Size 3.

(d) DNS model 4 (6x18x6 unit cells): Size 4.

Fig. 35. Geometry (3D view) and boundary conditions for DNS models ($L_x = L_z = 1$ mm and $L_y = 3$ mm).

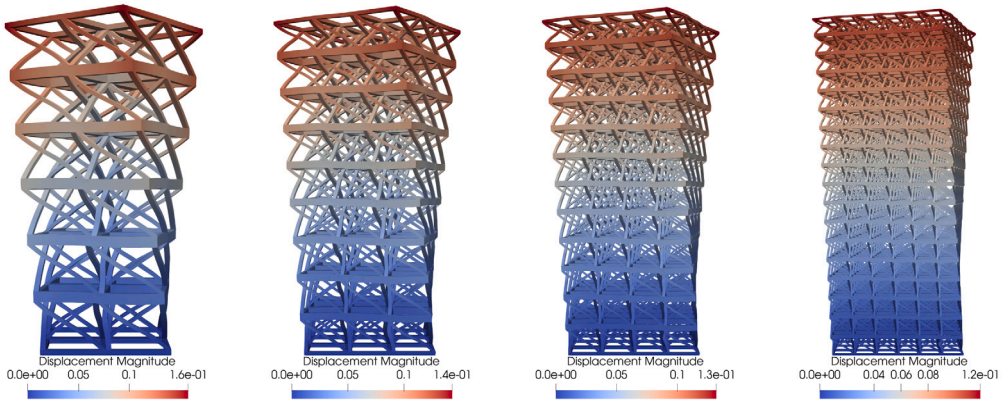

(a) DNS model 1.

(b) DNS model 2.

(c) DNS model 3.

(d) DNS model 4.

Fig. 36. Modulus of the displacement vector field for DNS models in a front view (scale factor = 4).

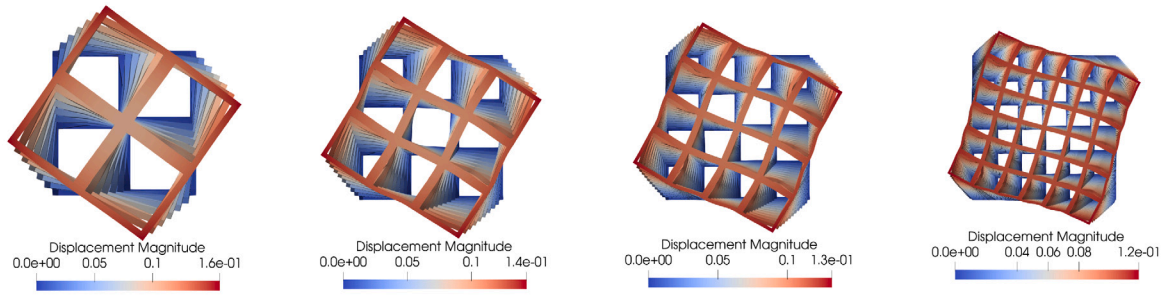

(a) DNS model 1. (b) DNS model 2. (c) DNS model 3. (d) DNS model 4.

Fig. 37. Modulus of the displacement vector field for DNS models in a top view (scale factor = 4).

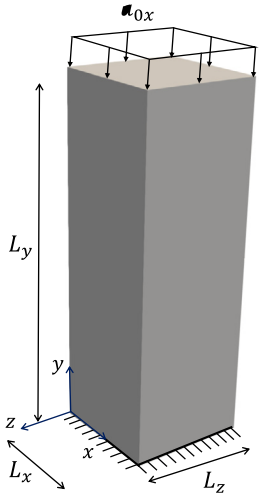

Fig. 38. Geometry (3D view) and boundary conditions ($L_x = L_z = 1$ mm and $L_y = 3$ mm).

3.4.2. Multi-scale simulations

Regarding the multi-scale simulations based on second-order homogenisation, only the minimal constraint was considered to discuss the results. Note that the periodic constraint is not applicable due to the geometry of the RVE. Moreover, the direct constraint did not adequately capture the compression-induced twisting because of the significantly stiffer homogenised behaviour. For comparison purposes, the classical uniform traction boundary condition derived from first-order homogenisation was also investigated.

The geometry and mesh of the RVE are shown in Fig. 34. Concerning the macro-scale problem, the geometry and boundary conditions are depicted in Fig. 38. Mixed hexahedral elements with 20 nodes (H20F8L1) and 8 integration points are employed in the finite element discretisation at the macro-scale (Rodrigues Lopes and Andrade Pires, 2022b). Three macro-scale meshes shown in Fig. 39 were adopted to evaluate mesh convergence. Fig. 41 presents the results of the mesh refinement study for $l_\mu = 0.500$ mm accounting for the rotation angle (θ) of the deformed structure (see Fig. 40). In summary, the results are close for all meshes investigated, indicating mesh convergence.

Towards multi-scale analyses, seven RVE lengths were investigated: $l_\mu = 0.500$ mm (size 1), $l_\mu = 0.333$ mm (size 2), $l_\mu = 0.250$ mm (size 3), $l_\mu = 0.167$ mm (size 4), $l_\mu = 0.125$ mm (size 5), $l_\mu = 0.100$ mm (size 6) and $l_\mu = 0.083$ mm (size 7). The results associated with the rotation angle (θ) of the deformed structure (see Fig. 40) for all RVE lengths are presented in Fig. 42. The deformed macro-scale structures for some RVE lengths are shown in Fig. 43 (front view) and Fig. 44 (top view) to compare results with DNS models. In addition, Fig. 45 shows the distribution of the effective Cauchy stress (MPa) for the deformed RVE ($l_\mu = 0.500$ mm) associated with the integration point I_B at macro-scale mesh 1 (see approximate region indicated in Fig. 39(a)). The first-order multi-scale analyses performed with the uniform traction boundary condition did not capture the rotation of the structure. Although quantitative differences compared to DNS models, the second-order multi-scale minimal constraint based on second-order homogenisation captures the compression-induced torsion at the macro-scale. It is worth highlighting the deformed RVE in Fig. 45, where the effect of torsion is clear at the micro-scale.

Following the discussion for DNS models, the reduction of the rotation angle for smaller RVE lengths was also captured in the coupled second-order multi-scale simulations with minimal constraint. Thus, the computational approach via second-order homogenisation captures the size effect of the metamaterial with compression–torsion coupling. Furthermore, a non-linear behaviour is observed in the curves relating θ and the RVE length.

3.4.3. Analysis of the homogenised properties

The consistent tangents required to solve the coupled multi-scale problem are important for understanding the compression-induced torsion observed for the metamaterial. In particular, the so-called coupling tangents are more relevant to explain the coupling deformation mechanism of torsion (second-order deformation mode) associated with compression (first-order deformation mode). Concerning the cross-relations established by these consistent tangents, $\mathbf{A_G}$ (A_{Gijklm}) associates $\boldsymbol{P}$ (P_{ij}) and $\mathbf{G}$ (G_{klm}):

$$A_{Gijklm} = \frac{\partial P_{ij}}{\partial G_{klm}}, \tag{35}$$

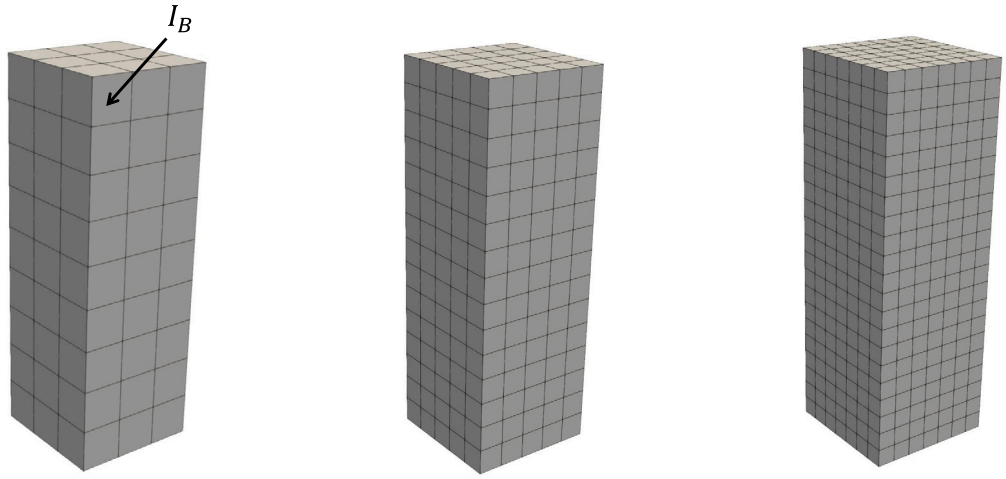

(a) Mesh 1: 81 elements (H20F8L1) and 544 nodes. (b) Mesh 2: 375 elements (H20F8L1) and 2076 nodes. (c) Mesh 3: 1029 elements (H20F8L1) and 5216 nodes.

Fig. 39. Macro-scale meshes.

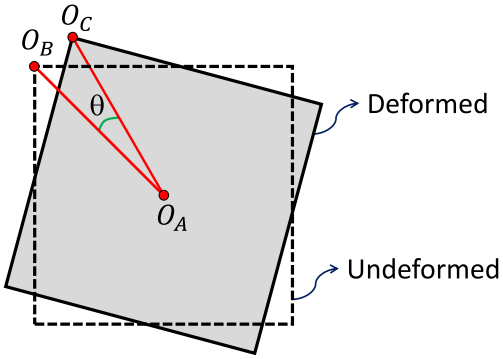

Fig. 40. Rotation angle (θ) for a top view of the structure.

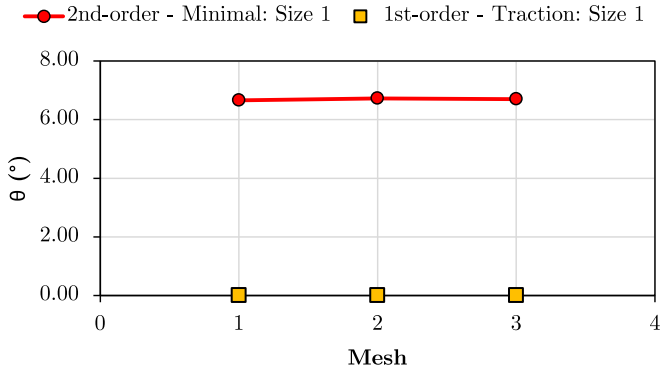

Fig. 41. Mesh study for RVE size 1 (l_μ = 0.500 mm) accounting for the rotation angle (θ): second-order minimal constraint (2nd-order — Minimal: Size 1) and first-order uniform traction boundary condition (1st-order — Traction: Size 1).

and $\mathbf{H}_F$ (H_{Fijklm}) relates $\mathbf{Q}$ (Q_{ijk}) and $\boldsymbol{F}$ (F_{lm}):

$$H_{Fijklm} = \frac{\partial Q_{ijk}}{\partial F_{lm}}. \tag{36}$$

In this context, Fig. 46 shows the norms of the initial consistent tangents $|\mathbf{A}_\mathbf{G}|$ and $|\mathbf{H}_F|$ of RVEs required for the FE^2 framework with minimal constraint related to second-order homogenisation. The non-null values for the consistent tangents indicate their contribution to the solution of the multi-scale problem based on second-order homogenisation. It is worth mentioning that there is a linear relationship between the norm of consistent tangents and the RVE length. On the other hand, these particular tangents are not considered in the solution for the uniform traction boundary condition related to the multi-scale

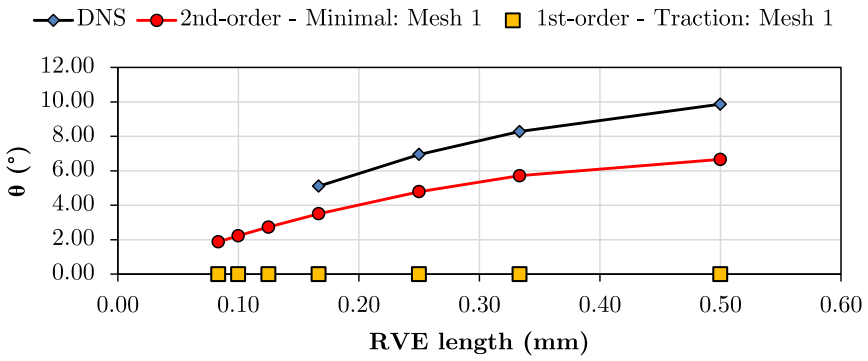

Fig. 42. RVE length x rotation angle: second-order minimal constraint with macro-scale mesh 1 (2nd-order — Minimal: Mesh 1) and first-order uniform traction boundary condition with macro-scale mesh 1 (1st-order — Traction: Mesh 1).

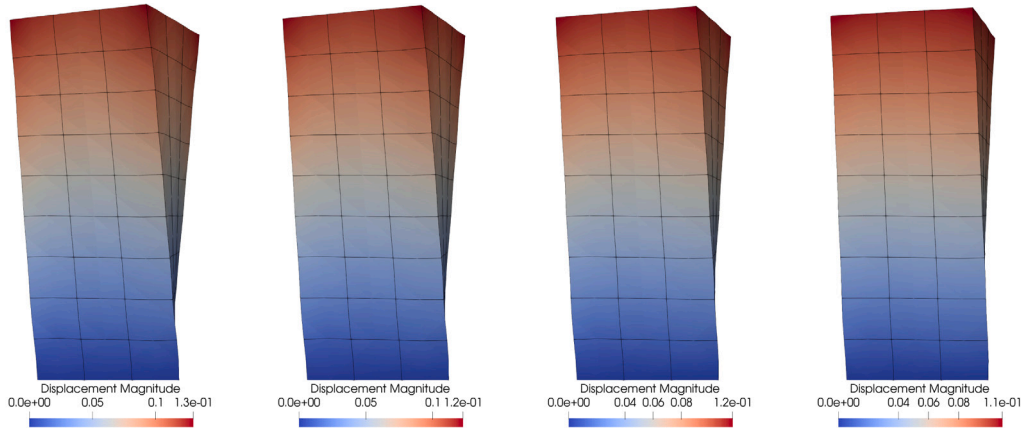

(a) Size 1: $l_\mu = 0.500$ mm. (b) Size 2: $l_\mu = 0.333$ mm. (c) Size 3: $l_\mu = 0.250$ mm. (d) Size 4: $l_\mu = 0.167$ mm.

Fig. 43. Modulus of the displacement vector field in mm for macro-scale structures (front view): Second-order — Minimal (scale factor = 4).

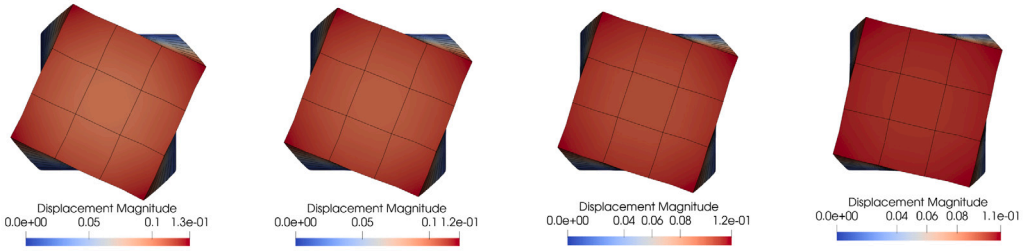

(a) Size 1: $l_\mu = 0.500$ mm. (b) Size 2: $l_\mu = 0.333$ mm. (c) Size 3: $l_\mu = 0.250$ mm. (d) Size 4: $l_\mu = 0.17$ mm.

Fig. 44. Modulus of the displacement vector field in mm for macro-scale structures (top view): Second-order — Minimal (scale factor = 4).

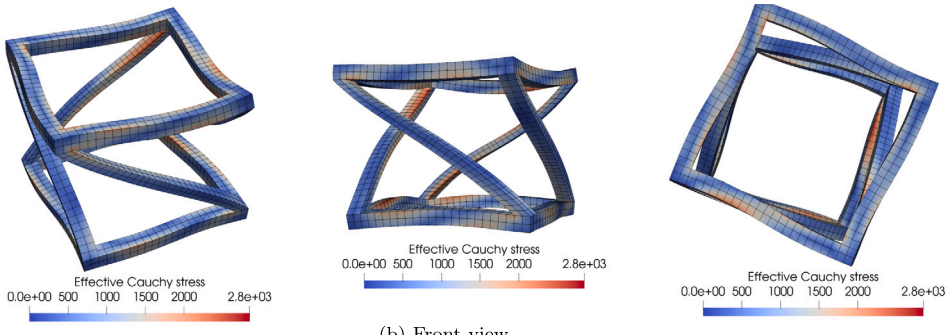

(a) Three-dimensional view. (b) Front view. (c) Top view.

Fig. 45. Effective Cauchy stress (MPa) for the deformed RVE (l_μ = 0.500 mm) associated with the integration point I_B at macro-scale mesh 1 (see approximate region indicated in Fig. 39(a)) for the multi-scale analysis via second-order computational homogenisation under the minimal constraint assumption (scale factor = 4).

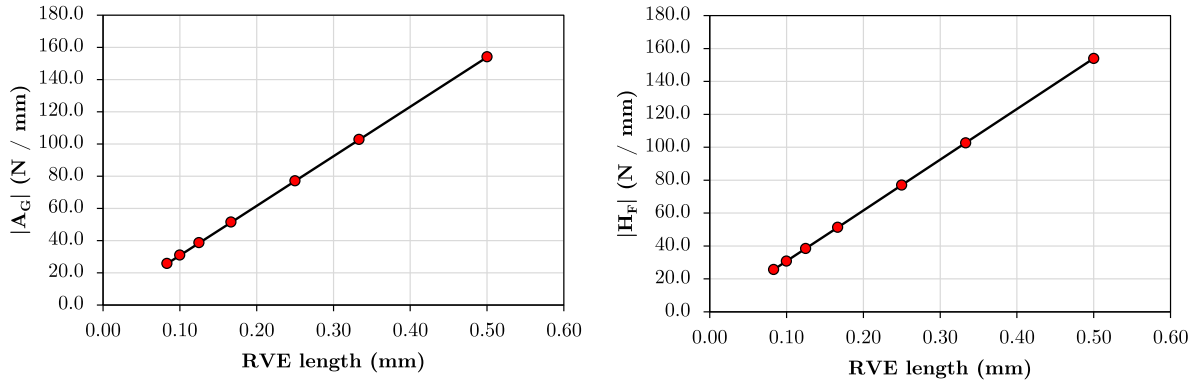

(a) Results for $|\mathbf{A_G}|$. (b) Results for $|\mathbf{H}_{\boldsymbol{F}}|$.

Fig. 46. Norm of consistent tangents required for the second-order multi-scale modelling with minimal constraint.

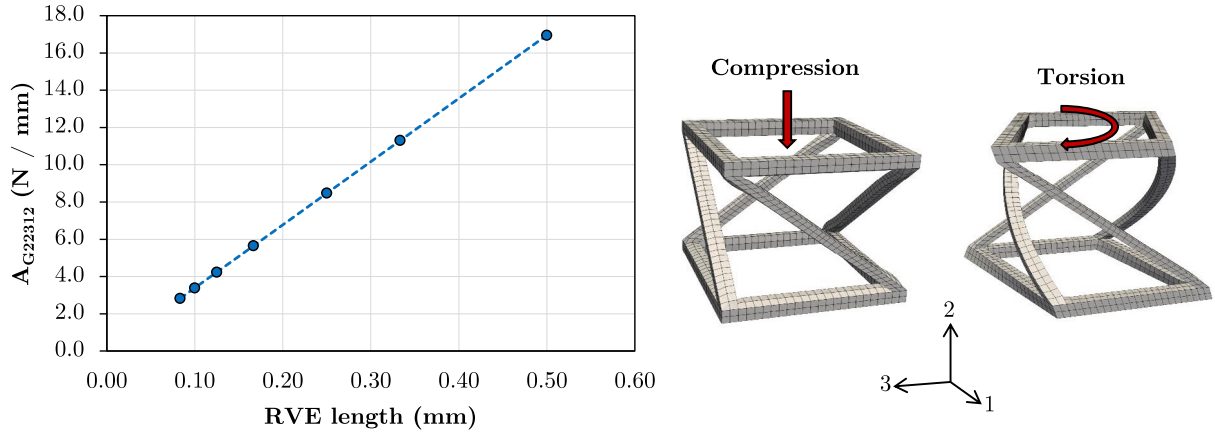

Fig. 47. Results for A_{G22312} component with coupling between normal stresses P_{22} and the torsion deformation mode G_{312}.

strategy based on first-order homogenisation, where the compression–torsion coupling was not captured. Therefore, $|\mathbf{A_G}|$ and $|\mathbf{H}_{\boldsymbol{F}}|$ were important for the second-order multi-scale approach to capture the effect of compression-induced torsion. For an in-depth discussion of the effect of compression-induced twisting, Fig. 47 presents the A_{G22312} component with coupling between normal stresses P_{22} and the torsion deformation mode G_{312}. Hence, the A_{G22312} component indicates the coupling between normal and torsional effects for the metamaterial.

4. Conclusions

In the present contribution, a multi-scale second-order computational homogenisation approach at finite strains was explored to investigate the macroscopic behaviour of architected materials and mechanical metamaterials. In order to demonstrate the robustness and applicability of the second-order computational approach, several numerical experiments were carefully investigated through two- or three-dimensional coupled multi-scale simulations conducted in an FE^2 framework. The numerical examples account for different loading programmes, including results associated with tension/compression-induced undulation, bending, and compression-induced torsion. The size effect due to the RVE length was assessed in all simulated structures. Moreover, the second-order approach was confronted with first-order theory and DNS models, and mesh convergence studies have also been performed.

Firstly, the behaviour of a novel mechanical metamaterial with tension/compression-induced undulation has been analysed. When subjected to tension or compression, its mechanical response is not influenced by the size effect associated with the length of the unit cell, as revealed in the numerical simulations with DNS models. Consequently, the multi-scale approaches based on first- and second-order computational homogenisation presented similar results for the mechanical behaviour of the metamaterial, capturing the tension/compression-induced undulation. Regarding the accuracy of the multi-scale models, periodic boundary conditions provided results in close agreement with the DNS models, resulting in better predictions compared to other classes of constraints. Moreover, the new exotic behaviour, which can be employed in shape-shifting applications associated with soft robotics and/or programmable materials, results from a non-conventional coupling between tension/compression and shear that is quantified in the material tangent modulus. This coupling is not associated with second-order deformation modes and, consequently, is accurately predicted by first-order homogenisation.

Secondly, numerical examples associated with bending highlighted significant advantages of second-order strategies, compared to classical first-order homogenisation. For two distinct architected materials, one modelled in a 2D framework, and another one with 3D models, the multi-scale second-order strategy presented responses in close agreement with the results from DNS, unlike the first-order approaches. The

size effects due to the RVE length revealed by DNS have been captured by the multi-scale approach based on second-order homogenisation.

Finally, it has been shown that multi-scale models based on second-order homogenisation can capture a complicated compression-induced torsion effect. A 3D RVE has been devised to induce this kind of effect and the corresponding DNS models reveal a size effect associated with the RVE length, that affects the torsional rotation. First-order homogenisation is not able to capture such deformation mode coupling. At the same time, multi-scale models based on second-order homogenisation can predict compression-induced torsion, as well as the associated size effect.

In summary, the simulated numerical examples showed that the second-order multi-scale strategy is capable of capturing relevant phenomena in more advanced materials, such as second-order deformation modes, coupling deformation mechanisms and size effects associated with microarchitecture length. In addition, the computational cost of solving DNS problems is alleviated with this kind of multi-scale approach, especially in what concerns memory requirements and for smaller sizes of the unit cell. Therefore, the developed computational framework can be useful in practical applications for designing cellular and lattice structures as well as mechanical metamaterials to obtain the desired macroscopic behaviour, encompassing remarkable or extreme properties and exotic functionalities. Nonetheless, when the exotic behaviour is based on the coupling between first-order deformation modes, first-order homogenisation is also adequate.

CRediT authorship contribution statement

Wanderson F. dos Santos: Conceptualization, Investigation, Methodology, Writing – original draft. **Igor A. Rodrigues Lopes:** Conceptualization, Formal analysis, Methodology, Writing – original draft, Writing – review & editing. **Francisco M. Andrade Pires:** Conceptualization, Investigation, Methodology, Supervision, Writing – review & editing. **Sergio P.B. Proença:** Conceptualization, Funding acquisition, Methodology, Supervision, Writing – review & editing.

Declaration of competing interest

The authors declare that they have no known competing financial interests or personal relationships that could have appeared to influence the work reported in this paper.

Data availability

No data was used for the research described in the article.

Acknowledgment

The first author acknowledges the support provided by Coordination for the Improvement of Higher Education Personnel (CAPES-Brazil).

References

Alavi, S., Ganghoffer, J., Sadighi, M., Nasimsobhan, M., Akbarzadeh, A., 2022. Continualization method of lattice materials and analysis of size effects revisited based on cosserat models. Int. J. Solids Struct. 254–255, 111894. http://dx.doi.org/10.1016/j.ijsolstr.2022.111894, URL https://www.sciencedirect.com/science/article/pii/S0020768322003584.

Alberdi, R., Dingreville, R., Robbins, J., Walsh, T., White, B.C., Jared, B., Boyce, B.L., 2020. Multi-morphology lattices lead to improved plastic energy absorption. Mater. Des. 194, 108883. http://dx.doi.org/10.1016/j.matdes.2020.108883, URL https://www.sciencedirect.com/science/article/pii/S0264127520304172.

An, X., Lai, C., He, W., Fan, H., 2021. Three-dimensional chiral meta-plate lattice structures for broad band vibration suppression and sound absorption. Composites B 224, 109232. http://dx.doi.org/10.1016/j.compositesb.2021.109232, URL https://www.sciencedirect.com/science/article/pii/S1359836821006090.

Babaee, S., Shim, J., Weaver, J.C., Chen, E.R., Patel, N., Bertoldi, K., 2013. 3D soft metamaterials with negative Poisson's ratio. Adv. Mater. 25 (36), 5044–5049. http://dx.doi.org/10.1002/adma.201301986, URL https://onlinelibrary.wiley.com/doi/abs/10.1002/adma.201301986. https://onlinelibrary.wiley.com/doi/pdf/10.1002/adma.201301986.

Bauer, J., Schwaiger, R., Kraft, O., 2016. Approaching theoretical strength in glassy carbon nanolattices. Nature Mater. 15 (4), 438–443. http://dx.doi.org/10.1038/nmat4561.

Baughman, R.H., Stafström, S., Cui, C., Dantas, S.O., 1998. Materials with negative compressibilities in one or more dimensions. Science 279 (5356), 1522–1524. http://dx.doi.org/10.1126/science.279.5356.1522, URL https://www.science.org/doi/abs/10.1126/science.279.5356.1522.

Benedetti, M., du Plessis, A., Ritchie, R., Dallago, M., Razavi, S., Berto, F., 2021. Architected cellular materials: A review on their mechanical properties towards fatigue-tolerant design and fabrication. Mater. Sci. Eng. R 144, 100606. http://dx.doi.org/10.1016/j.mser.2021.100606, URL https://www.sciencedirect.com/science/article/pii/S0927796X21000012.

Bertoldi, K., Boyce, M., Deschanel, S., Prange, S., Mullin, T., 2008. Mechanics of deformation-triggered pattern transformations and superelastic behavior in periodic elastomeric structures. J. Mech. Phys. Solids 56 (8), 2642–2668. http://dx.doi.org/10.1016/j.jmps.2008.03.006, URL https://www.sciencedirect.com/science/article/pii/S0022509608000434.

Bertoldi, K., Reis, P.M., Willshaw, S., Mullin, T., 2010. Negative Poisson's ratio behavior induced by an elastic instability. Adv. Mater. 22 (3), 361–366. http://dx.doi.org/10.1002/adma.200901956, URL https://onlinelibrary.wiley.com/doi/abs/10.1002/adma.200901956. https://onlinelibrary.wiley.com/doi/pdf/10.1002/adma.200901956.

Biswas, R., Poh, L.H., Shedbale, A.S., 2020. A micromorphic computational homogenization framework for auxetic tetra-chiral structures. J. Mech. Phys. Solids 135, 103801. http://dx.doi.org/10.1016/j.jmps.2019.103801, URL https://www.sciencedirect.com/science/article/pii/S0022509619307203.

Blanco, P.J., Sánchez, P.J., de Souza Neto, E.A., Feijóo, R.A., 2016a. Variational foundations and generalized unified theory of RVE-based multiscale models. Arch. Comput. Methods Eng. 23 (2), 191–253, URL http://link.springer.com/10.1007/s11831-014-9137-5.

Blanco, P., Sànchez, P., Neto, E.d., Feijòo, R., 2016b. The method of multiscale virtual power for the derivation of a second order mechanical model. Mech. Mater. 99, 53–67, URL http://www.sciencedirect.com/science/article/pii/S0167663616300400.

Blanco, P., Sánchez, P., Rocha, F., Toro, S., Feijóo, R., 2023. A consistent multiscale mechanical formulation for media with randomly distributed voids. Int. J. Solids Struct. 283, 112494. http://dx.doi.org/10.1016/j.ijsolstr.2023.112494, URL https://www.sciencedirect.com/science/article/pii/S0020768323003918.

Catchpole-Smith, S., Sélo, R., Davis, A., Ashcroft, I., Tuck, C., Clare, A., 2019. Thermal conductivity of TPMS lattice structures manufactured via laser powder bed fusion. Addit. Manuf. 30, 100846. http://dx.doi.org/10.1016/j.addma.2019.100846, URL https://www.sciencedirect.com/science/article/pii/S2214860419307559.

Chen, X., Ji, Q., Wei, J., Tan, H., Yu, J., Zhang, P., Laude, V., Kadic, M., 2020. Light-weight shell-lattice metamaterials for mechanical shock absorption. Int. J. Mech. Sci. 169, 105288. http://dx.doi.org/10.1016/j.ijmecsci.2019.105288, URL https://www.sciencedirect.com/science/article/pii/S0020740319313839.

Cheng, H., Zhu, X., Cheng, X., Cai, P., Liu, J., Yao, H., Zhang, L., Duan, J., 2023. Mechanical metamaterials made of freestanding quasi-BCC nanolattices of gold and copper with ultra-high energy absorption capacity. Nature Commun. 14 (5356), http://dx.doi.org/10.1038/s41467-023-36965-4.

Dos Reis, F., Ganghoffer, J., 2012. Construction of micropolar continua from the asymptotic homogenization of beam lattices. Comput. Struct. 112–113, 354–363. http://dx.doi.org/10.1016/j.compstruc.2012.08.006, URL https://www.sciencedirect.com/science/article/pii/S0045794912001940.

Dos Santos, W.F., Rodrigues Lopes, I.A., Andrade Pires, F.M., Proença, S.P., 2023. Second-order multi-scale modelling of natural and architected materials in the presence of voids: Formulation and numerical implementation. Comput. Methods Appl. Mech. Engrg. 416, 116374. http://dx.doi.org/10.1016/j.cma.2023.116374, URL https://www.sciencedirect.com/science/article/pii/S004578252300498X.

du Plessis, A., Razavi, N., Benedetti, M., Murchio, S., Leary, M., Watson, M., Bhate, D., Berto, F., 2022. Properties and applications of additively manufactured metallic cellular materials: A review. Prog. Mater. Sci. 125, 100918. http://dx.doi.org/10.1016/j.pmatsci.2021.100918, URL https://www.sciencedirect.com/science/article/pii/S0079642521001420.

Duan, S., Wen, W., Fang, D., 2018. A predictive micropolar continuum model for a novel three-dimensional chiral lattice with size effect and tension-twist coupling behavior. J. Mech. Phys. Solids 121, 23–46. http://dx.doi.org/10.1016/j.jmps.2018.07.016, URL https://www.sciencedirect.com/science/article/pii/S0022509618303016.

Fernandez-Corbaton, I., Rockstuhl, C., Ziemke, P., Gumbsch, P., Albiez, A., Schwaiger, R., Frenzel, T., Kadic, M., Wegener, M., 2019. New twists of 3D chiral metamaterials. Adv. Mater. 31 (26), 1807742. http://dx.doi.org/10.1002/adma.201807742, URL https://onlinelibrary.wiley.com/doi/abs/10.1002/adma.201807742. https://onlinelibrary.wiley.com/doi/pdf/10.1002/adma.201807742.

Frenzel, T., Hahn, V., Ziemke, P., Schneider, J.L.G., Chen, Y., Kiefer, P., Gumbsch, P., Wegener, M., 2021. Large characteristic lengths in 3D chiral elastic metamaterials. Commun. Mater. 2, http://dx.doi.org/10.1038/s43246-020-00107-w.

Frenzel, T., Kadic, M., Wegener, M., 2017. Three-dimensional mechanical metamaterials with a twist. Science 358 (6366), 1072–1074. http://dx.doi.org/10.1126/science.aao4640, URL https://www.science.org/doi/abs/10.1126/science.aao4640. https://www.science.org/doi/pdf/10.1126/science.aao4640.

Ganghoffer, J.-F., Wazne, A., Reda, H., 2023. Frontiers in homogenization methods towards generalized continua for architected materials. Mech. Res. Commun. 130, 104114. http://dx.doi.org/10.1016/j.mechrescom.2023.104114, URL https://www.sciencedirect.com/science/article/pii/S0093641323000721.

Gao, C., Slesarenko, V., Boyce, M.C., Rudykh, S., Li, Y., 2018. Instability-induced pattern transformation in soft metamaterial with hexagonal networks for tunable wave propagation. Sci. Rep. 8 (1), 2045–2322. http://dx.doi.org/10.1038/s41598-018-30381-1.

Gatt, R., Grima, J.N., 2008. Negative compressibility. Phys. Status Solidi (RRL) – Rapid Res. Lett. 2 (5), 236–238. http://dx.doi.org/10.1002/pssr.200802101, URL https://onlinelibrary.wiley.com/doi/abs/10.1002/pssr.200802101.

Geers, M.G.D., Kouznetsova, V.G., Brekelmans, W.A.M., 2003. MultiScale first-order and second-order computational homogenization of microstructures towards continua. Int. J. Multiscale Comput. Eng. 4, 371–386. http://dx.doi.org/10.1615/IntJMultCompEng.v1.i4.40.

Guo, W., Huang, Y., Ritchie, R.O., Yin, S., 2021. Dissipative dual-phase mechanical metamaterial composites via architectural design. Extreme Mech. Lett. 48, 101442. http://dx.doi.org/10.1016/j.eml.2021.101442, URL https://www.sciencedirect.com/science/article/pii/S2352431621001590.

Hii, A.K., El Said, B., 2022. A kinematically consistent second-order computational homogenisation framework for thick shell models. Comput. Methods Appl. Mech. Engrg. 398, 115136. http://dx.doi.org/10.1016/j.cma.2022.115136, URL https://www.sciencedirect.com/science/article/pii/S0045782522003139.

Hosseini, S., Niiranen, J., 2022. 3D strain gradient elasticity: Variational formulations, isogeometric analysis and model peculiarities. Comput. Methods Appl. Mech. Engrg. 389, 114324. http://dx.doi.org/10.1016/j.cma.2021.114324, URL https://www.sciencedirect.com/science/article/pii/S0045782521006149.

Jia, Z., Liu, F., Jiang, X., Wang, L., 2020. Engineering lattice metamaterials for extreme property, programmability, and multifunctionality. J. Appl. Phys. 127 (15), 150901. http://dx.doi.org/10.1063/5.0004724.

Jiao, P., Mueller, J., Raney, J.R., Zheng, X.R., Alavi, A.H., 2023. Mechanical metamaterials and beyond. Nature Commun. 14 (1), http://dx.doi.org/10.1038/s41467-023-41679-8.

Kaczmarczyk, Ł., Pearce, C.J., Bićanić, N., 2008. Scale transition and enforcement of RVE boundary conditions in second-order computational homogenization. Internat. J. Numer. Methods Engrg. 74 (3), 506–522, URL http://doi.wiley.com/10.1002/nme.2188.

Kaczmarczyk, Ł., Pearce, C.J., Bićanić, N., 2010. Studies of microstructural size effect and higher-order deformation in second-order computational homogenization. Comput. Struct. 88 (23–24), 1383–1390, URL http://linkinghub.elsevier.com/retrieve/pii/S0045794908001922.

Kang, D., Park, S., Son, Y., Yeon, S., Kim, S.H., Kim, I., 2019. Multi-lattice inner structures for high-strength and light-weight in metal selective laser melting process. Mater. Des. 175, 107786. http://dx.doi.org/10.1016/j.matdes.2019.107786, URL https://www.sciencedirect.com/science/article/pii/S0264127519302230.

Khakalo, S., Balobanov, V., Niiranen, J., 2018. Modelling size-dependent bending, buckling and vibrations of 2D triangular lattices by strain gradient elasticity models: Applications to sandwich beams and auxetics. Internat. J. Engrg. Sci. 127, 33–52. http://dx.doi.org/10.1016/j.ijengsci.2018.02.004, URL https://www.sciencedirect.com/science/article/pii/S0020722517319535.

Kouznetsova, V., Geers, M., Brekelmans, W., 2004a. Multi-scale second-order computational homogenization of multi-phase materials: a nested finite element solution strategy. Comput. Methods Appl. Mech. Engrg. 193 (48–51), 5525–5550. http://dx.doi.org/10.1016/j.cma.2003.12.073, URL https://www.sciencedirect.com/science/article/pii/S0045782504002853.

Kouznetsova, V.G., Geers, M.G.D., Brekelmans, W.A.M., 2004b. Size of a representative volume element in a second-order computational homogenization framework. Int. J. Multiscale Comput. Eng. 2 (4), 575–598. http://dx.doi.org/10.1615/IntJMultCompEng.v2.i4.50.

Kumar, R.S., McDowell, D.L., 2004. Generalized continuum modeling of 2-D periodic cellular solids. Int. J. Solids Struct. 41 (26), 7399–7422. http://dx.doi.org/10.1016/j.ijsolstr.2004.06.038, URL https://www.sciencedirect.com/science/article/pii/S0020768304003658.

Lakes, R., 1987. Foam structures with a negative Poisson's ratio. Science 235 (4792), 1038–1040. http://dx.doi.org/10.1126/science.235.4792.1038, URL https://www.science.org/doi/abs/10.1126/science.235.4792.1038.

Lakes, R.S., Lee, T., Bersie, A., Wang, Y.C., 2012. Extreme damping in composite materials with negative-stiffness inclusions. Nature 410 (6828), 565–567. http://dx.doi.org/10.1038/35069035.

Lemkalli, B., Kadic, M., El Badri, Y., Guenneau, S., Bouzid, A., Achaoui, Y., 2023. Mapping of elastic properties of twisting metamaterials onto micropolar continuum using static calculations. Int. J. Mech. Sci. 254, 108411. http://dx.doi.org/10.1016/j.ijmecsci.2023.108411, URL https://www.sciencedirect.com/science/article/pii/S0020740323003132.

Lesičar, T., Sorić, J., Tonković, Z., 2016. Large strain, two-scale computational approach using C1 continuity finite element employing a second gradient theory. Comput. Methods Appl. Mech. Engrg. 298, 303–324. http://dx.doi.org/10.1016/j.cma.2015.09.017, URL https://www.sciencedirect.com/science/article/pii/S0045782515003114.

Lesičar, T., Tonković, Z., Sorić, J., 2014. A second-order two-scale homogenization procedure using C1 macrolevel discretization. Comput. Mech. 54, 425–441. http://dx.doi.org/10.1007/s00466-014-0995-3.

Lesičar, T., Tonković, Z., Sorić, J., 2017. Two-scale computational approach using strain gradient theory at microlevel. Int. J. Mech. Sci. 126, 67–78. http://dx.doi.org/10.1016/j.ijmecsci.2017.02.017, URL http://www.sciencedirect.com/science/article/pii/S0020740316304258.

Li, X., Gao, H., 2016. Smaller and stronger. Nature Mater. 15 (4), 373–374. http://dx.doi.org/10.1038/nmat4591.

Li, Z., Li, X., Chua, J.W., Lim, C.H., Yu, X., Wang, Z., Zhai, W., 2023. Architected lightweight, sound-absorbing, and mechanically efficient microlattice metamaterials by digital light processing 3D printing. Virtual Phys. Prototyp. 18 (1), e2166851. http://dx.doi.org/10.1080/17452759.2023.2166851.

Luscher, D.J., McDowell, D.L., Bronkhorst, C.A., 2010. A second gradient theoretical framework for hierarchical multiscale modeling of materials. Int. J. Plast. 26 (8), 1248–1275. http://dx.doi.org/10.1016/j.ijplas.2010.05.006, URL https://www.sciencedirect.com/science/article/pii/S0749641910000719.

Luscher, D.J., McDowell, D.L., Bronkhorst, C.A., 2012. Essential features of fine scale boundary conditions for second gradient multiscale homogenization of statistical volume elements. Int. J. Multiscale Comput. Eng. 10 (5), 461–486. http://dx.doi.org/10.1615/IntJMultCompEng.2012002929, URL https://www.dl.begellhouse.com/journals/61fd1b191cf7e96f,58ae1c03228f5d43,22758e010b9fed16.html.

Meza, L.R., Das, S., Greer, J.R., 2014. Strong, lightweight, and recoverable three-dimensional ceramic nanolattices. Science 345 (6202), 1322–1326. http://dx.doi.org/10.1126/science.1255908, URL https://www.science.org/doi/abs/10.1126/science.1255908.

Mizzi, L., Mahdi, E., Titov, K., Gatt, R., Attard, D., Evans, K.E., Grima, J.N., Tan, J.-C., 2018. Mechanical metamaterials with star-shaped pores exhibiting negative and zero Poisson's ratio. Mater. Des. 146, 28–37. http://dx.doi.org/10.1016/j.matdes.2018.02.051, URL https://www.sciencedirect.com/science/article/pii/S0264127518301424.

Molavitabrizi, D., Khakalo, S., Bengtsson, R., Mousavi, S.M., 2023. Second-order homogenization of 3-D lattice materials towards strain gradient media: numerical modelling and experimental verification. Contin. Mech. Thermodyn. http://dx.doi.org/10.1007/s00161-023-01246-4, URL https://link.springer.com/article/10.1007/s00161-023-01246-4.

Mukhopadhyay, T., Adhikari, S., 2016. Effective in-plane elastic properties of auxetic honeycombs with spatial irregularity. Mech. Mater. 95, 204–222. http://dx.doi.org/10.1016/j.mechmat.2016.01.009, URL https://www.sciencedirect.com/science/article/pii/S0167663616000181.

Mullin, T., 2007. Pattern transformation triggered by deformation. Phys. Rev. Lett. 99, 084301. http://dx.doi.org/10.1103/PhysRevLett.99.084301.

Nguyen, V.D., Becker, G., Noels, L., 2013. Multiscale computational homogenization methods with a gradient enhanced scheme based on the discontinuous Galerkin formulation. Comput. Methods Appl. Mech. Engrg. 260, 63–77. http://dx.doi.org/10.1016/j.cma.2013.03.024, URL https://www.sciencedirect.com/science/article/pii/S0045782513000832.

Nguyen, V.-D., Noels, L., 2014. Computational homogenization of cellular materials. Int. J. Solids Struct. 51 (11–12), 2183–2203.

Nicolaou, Z.G., Motter, A.E., 2012. Mechanical metamaterials with negative compressibility transitions. Nature Mater. 11 (7), 608–613. http://dx.doi.org/10.1038/nmat3331.

Pan, C., Han, Y., Lu, J., 2020. Design and optimization of lattice structures: A review. Appl. Sci. 10 (18), http://dx.doi.org/10.3390/app10186374, URL https://www.mdpi.com/2076-3417/10/18/6374.

Qi, C., Jiang, F., Yang, S., 2021. Advanced honeycomb designs for improving mechanical properties: A review. Composites B 227, 109393. http://dx.doi.org/10.1016/j.compositesb.2021.109393, URL https://www.sciencedirect.com/science/article/pii/S1359836821007642.

Qi, D., Zhang, P., Wu, W., Xin, K., Liao, H., Li, Y., Xiao, D., Xia, R., 2020. Innovative 3D chiral metamaterials under large deformation: Theoretical and experimental analysis. Int. J. Solids Struct. 202, 787–797. http://dx.doi.org/10.1016/j.ijsolstr.2020.06.047, URL https://www.sciencedirect.com/science/article/pii/S0020768320302699.

Reis, F., Andrade Pires, F.M., 2013. An adaptive sub-incremental strategy for the solution of homogenization-based multi-scale problems. Comput. Methods Appl. Mech. Engrg. 257, 164–182. http://dx.doi.org/10.1016/j.cma.2013.01.003, URL https://www.sciencedirect.com/science/article/pii/S0045782513000078.

Rico-Baeza, G., Cuan-Urquizo, E., Pérez-Soto, G.I., Alcaraz-Caracheo, L.A., Camarillo-Gómez, K.A., 2023. Additively manufactured lattice materials with a double level of gradation: A comparison of their compressive properties when fabricated with material extrusion and vat photopolymerization processes. Materials 16 (2), http://dx.doi.org/10.3390/ma16020649, URL https://www.mdpi.com/1996-1944/16/2/649.

Rifaie, M.A., Abdulhadi, H., Mian, A., 2022. Advances in mechanical metamaterials for vibration isolation: A review. Adv. Mech. Eng. 14 (3), 16878132221082872. http://dx.doi.org/10.1177/16878132221082872.

Rocha, F.F., Blanco, P.J., Sánchez, P.J., Feijóo, R.A., 2018. Multi-scale modelling of arterial tissue: Linking networks of fibres to continua. Comput. Methods Appl. Mech. Engrg. 341, 740–787. http://dx.doi.org/10.1016/j.cma.2018.06.031, URL https://www.sciencedirect.com/science/article/pii/S0045782518303281.

Rodrigues Lopes, I.A., Andrade Pires, F.M., 2022a. An assessment of multi-scale models based on second-order computational homogenisation. Comput. Struct. 259, 106679. http://dx.doi.org/10.1016/j.compstruc.2021.106679, URL https://www.sciencedirect.com/science/article/pii/S0045794921002017.

Rodrigues Lopes, I.A., Andrade Pires, F.M., 2022b. Formulation and numerical implementation of a variationally consistent multi-scale model based on second-order computational homogenisation at finite strains for quasi-static problems. Comput. Methods Appl. Mech. Engrg. 392, 114714. http://dx.doi.org/10.1016/j.cma.2022.114714, URL https://www.sciencedirect.com/science/article/pii/S0045782522000834.

Rodrigues Lopes, I.A., Andrade Pires, F.M., 2022c. A fully second-order homogenization formulation for the multi-scale modeling of heterogeneous materials. Internat. J. Numer. Methods Engrg. 123 (21), 5274–5318. http://dx.doi.org/10.1002/nme.7063, URL https://onlinelibrary.wiley.com/doi/abs/10.1002/nme.7063.

Rodrigues Lopes, I.A., Andrade Pires, F.M., 2022d. Unlocking the potential of second-order computational homogenisation: An overview of distinct formulations and a guide for their implementation. Arch. Comput. Methods Eng. 29, 1339–1393. http://dx.doi.org/10.1007/s11831-021-09611-9.

Rodrigues Lopes, I.A., Ferreira, B.P., Andrade Pires, F.M., 2021. On the efficient enforcement of uniform traction and mortar periodic boundary conditions in computational homogenisation. Comput. Methods Appl. Mech. Engrg. 384, 113930. http://dx.doi.org/10.1016/j.cma.2021.113930, URL https://www.sciencedirect.com/science/article/pii/S004578252100267X.

Rokoš, O., Ameen, M., Peerlings, R., Geers, M., 2019. Micromorphic computational homogenization for mechanical metamaterials with patterning fluctuation fields. J. Mech. Phys. Solids 123, 119–137, URL https://www.sciencedirect.com/science/article/pii/S0022509618306148?via{%}3Dihub.

Rokoš, O., Ameen, M., Peerlings, R., Geers, M., 2020. Extended micromorphic computational homogenization for mechanical metamaterials exhibiting multiple geometric pattern transformations. Extreme Mech. Lett. 37, 100708. http://dx.doi.org/10.1016/j.eml.2020.100708, URL https://www.sciencedirect.com/science/article/pii/S2352431620300699.

Sajjad, U., ur Rehman, T., Ali, M., Park, C.W., Yan, W.-M., 2022. Manufacturing and potential applications of lattice structures in thermal systems: A comprehensive review of recent advances. Int. J. Heat Mass Transfer 198, 123352. http://dx.doi.org/10.1016/j.ijheatmasstransfer.2022.123352, URL https://www.sciencedirect.com/science/article/pii/S0017931022008225.

Sarhil, M., Scheunemann, L., Schröder, J., Neff, P., 2023. Size-effects of metamaterial beams subjected to pure bending: on boundary conditions and parameter identification in the relaxed micromorphic model. Comput. Mech. http://dx.doi.org/10.1007/s00466-023-02332-9.

Schaedler, T.A., Jacobsen, A.J., Torrents, A., Sorensen, A.E., Lian, J., Greer, J.R., Valdevit, L., Carter, W.B., 2011. Ultralight metallic microlattices. Science 334 (6058), 962–965. http://dx.doi.org/10.1126/science.1211649, URL https://www.science.org/doi/abs/10.1126/science.1211649.

Schmidt, F., Krüger, M., Keip, M.-A., Hesch, C., 2022. Computational homogenization of higher-order continua. Internat. J. Numer. Methods Engrg. 123 (11), 2499–2529. http://dx.doi.org/10.1002/nme.6948, URL https://onlinelibrary.wiley.com/doi/abs/10.1002/nme.6948.

Song, J., Zhou, W., Wang, Y., Fan, R., Wang, Y., Chen, J., Lu, Y., Li, L., 2019. Octet-truss cellular materials for improved mechanical properties and specific energy absorption. Mater. Des. 173, 107773. http://dx.doi.org/10.1016/j.matdes.2019.107773, URL https://www.sciencedirect.com/science/article/pii/S0264127519302102.

Su, Y., Wu, X., Shi, J., 2022. A novel 3D printable multimaterial auxetic metamaterial with reinforced structure: Improved stiffness and retained auxetic behavior. Mech. Adv. Mater. Struct. 29 (3), 408–418. http://dx.doi.org/10.1080/15376494.2020.1774690, arXiv:https://doi.org/10.1080/15376494.2020.1774690.

Surjadi, J.U., Gao, L., Du, H., Li, X., Xiong, X., Fang, N.X., Lu, Y., 2019. Mechanical metamaterials and their engineering applications. Adv. Eng. Mater. 21 (3), 1800864. http://dx.doi.org/10.1002/adem.201800864, URL https://onlinelibrary.wiley.com/doi/abs/10.1002/adem.201800864. https://onlinelibrary.wiley.com/doi/pdf/10.1002/adem.201800864.

Syam, W.P., Jianwei, W., Zhao, B., Maskery, I., Elmadih, W., Leach, R., 2018. Design and analysis of strut-based lattice structures for vibration isolation. Precis. Eng. 52, 494–506. http://dx.doi.org/10.1016/j.precisioneng.2017.09.010, URL https://www.sciencedirect.com/science/article/pii/S0141635917302726.

van Bree, S., Rokoš, O., Peerlings, R., Doškář, M., Geers, M., 2020. A Newton solver for micromorphic computational homogenization enabling multiscale buckling analysis of pattern-transforming metamaterials. Comput. Methods Appl. Mech. Engrg. 372, 113333. http://dx.doi.org/10.1016/j.cma.2020.113333, URL https://www.sciencedirect.com/science/article/pii/S0045782520305181.

Vazic, B., Newell, P., 2023. Towards the design of nature-inspired materials: Impact of complex pore morphologies via higher-order homogenization. Mech. Mater. 181, 104641. http://dx.doi.org/10.1016/j.mechmat.2023.104641, URL https://www.sciencedirect.com/science/article/pii/S016766362300087X.

Wang, L., Liu, H.-T., 2020. 3D compression–torsion cubic mechanical metamaterial with double inclined rods. Extreme Mech. Lett. 37, 100706. http://dx.doi.org/10.1016/j.eml.2020.100706, URL https://www.sciencedirect.com/science/article/pii/S2352431620300687.

Weeger, O., 2021. Numerical homogenization of second gradient, linear elastic constitutive models for cubic 3D beam-lattice metamaterials. Int. J. Solids Struct. 224, 111037. http://dx.doi.org/10.1016/j.ijsolstr.2021.03.024, URL https://www.sciencedirect.com/science/article/pii/S0020768321001153.

Wu, W., Hu, W., Qian, G., Liao, H., Xu, X., Berto, F., 2019. Mechanical design and multifunctional applications of chiral mechanical metamaterials: A review. Mater. Des. 180, 107950. http://dx.doi.org/10.1016/j.matdes.2019.107950, URL https://www.sciencedirect.com/science/article/pii/S0264127519303880.

Wu, L., Mustafa, M., Segurado, J., Noels, L., 2023. Second-order computational homogenisation enhanced with non-uniform body forces for non-linear cellular materials and metamaterials. Comput. Methods Appl. Mech. Engrg. 407, 115931. http://dx.doi.org/10.1016/j.cma.2023.115931, URL https://www.sciencedirect.com/science/article/pii/S0045782523000543.

Xu, W., Wang, L., Liu, Z., Zhu, P., 2023. General assembly rules for metamaterials with scalable twist effects. Int. J. Mech. Sci. 259, 108579. http://dx.doi.org/10.1016/j.ijmecsci.2023.108579, URL https://www.sciencedirect.com/science/article/pii/S0020740323004812.

Yang, H., Abali, B.E., Müller, W.H., Barboura, S., Li, J., 2022. Verification of asymptotic homogenization method developed for periodic architected materials in strain gradient continuum. Int. J. Solids Struct. 238, 111386. http://dx.doi.org/10.1016/j.ijsolstr.2021.111386, URL https://www.sciencedirect.com/science/article/pii/S0020768321004510.

Yang, H., Abali, B.E., Timofeev, D., Müller, W.H., 2020. Determination of metamaterial parameters by means of a homogenization approach based on asymptotic analysis. Contin. Mech. Thermodyn. 32, http://dx.doi.org/10.1007/s00161-019-00837-4.

Yang, H., Müller, W.H., 2021. Size effects of mechanical metamaterials: a computational study based on a second-order asymptotic homogenization method. Arch. Appl. Mech. 91, http://dx.doi.org/10.1007/s00419-020-01808-x.

Yang, H., Timofeev, D., Giorgio, I., Müller, W.H., 2021. Effective strain gradient continuum model of metamaterials and size effects analysis. Contin. Mech. Thermodyn. 35, http://dx.doi.org/10.1007/s00161-020-00910-3.

Yin, H., Zhang, W., Zhu, L., Meng, F., Liu, J., Wen, G., 2023. Review on lattice structures for energy absorption properties. Compos. Struct. 304, 116397. http://dx.doi.org/10.1016/j.compstruct.2022.116397, URL https://www.sciencedirect.com/science/article/pii/S0263822322011291.

Yoder, M., Thompson, L., Summers, J., 2018. Size effects in lattice structures and a comparison to micropolar elasticity. Int. J. Solids Struct. 143, 245–261. http://dx.doi.org/10.1016/j.ijsolstr.2018.03.013, URL https://www.sciencedirect.com/science/article/pii/S0020768318301215.

Yu, X., Zhou, J., Liang, H., Jiang, Z., Wu, L., 2018. Mechanical metamaterials associated with stiffness, rigidity and compressibility: A brief review. Prog. Mater. Sci. 94, 114–173. http://dx.doi.org/10.1016/j.pmatsci.2017.12.003, URL https://www.sciencedirect.com/science/article/pii/S0079642517301445.

Yvonnet, J., Auffray, N., Monchiet, V., 2020. Computational second-order homogenization of materials with effective anisotropic strain-gradient behavior. Int. J. Solids Struct. 191–192, 434–448. http://dx.doi.org/10.1016/j.ijsolstr.2020.01.006, URL https://www.sciencedirect.com/science/article/pii/S0020768320300123.

Zhang, X.Y., Ren, X., Zhang, Y., Xie, Y.M., 2022. A novel auxetic metamaterial with enhanced mechanical properties and tunable auxeticity. Thin-Walled Struct. 174, 109162. http://dx.doi.org/10.1016/j.tws.2022.109162, URL https://www.sciencedirect.com/science/article/pii/S0263823122001501.

Zhang, X., Vyatskikh, A., Gao, H., Greer, J.R., Li, X., 2019. Lightweight, flaw-tolerant, and ultrastrong nanoarchitected carbon. Proc. Natl. Acad. Sci. 116 (14), 6665–6672. http://dx.doi.org/10.1073/pnas.1817309116, URL https://www.pnas.org/doi/abs/10.1073/pnas.1817309116.

Zheng, X., Lee, H., Weisgraber, T.H., Shusteff, M., DeOtte, J., Duoss, E.B., Kuntz, J.D., Biener, M.M., Ge, Q., Jackson, J.A., Kucheyev, S.O., Fang, N.X., Spadaccini, C.M., 2014. Ultralight, ultrastiff mechanical metamaterials. Science 344 (6190), 1373–1377. http://dx.doi.org/10.1126/science.1252291, URL https://www.science.org/doi/abs/10.1126/science.1252291.

Zheng, B.-B., Zhong, R.-C., Chen, X., Fu, M.-H., Hu, L.-L., 2019. A novel metamaterial with tension-torsion coupling effect. Mater. Des. 171, 107700. http://dx.doi.org/10.1016/j.matdes.2019.107700, URL https://www.sciencedirect.com/science/article/pii/S0264127519301376.

Zhong, R., Fu, M., Chen, X., Zheng, B., Hu, L., 2019. A novel three-dimensional mechanical metamaterial with compression-torsion properties. Compos. Struct. 226, 111232. http://dx.doi.org/10.1016/j.compstruct.2019.111232, URL https://www.sciencedirect.com/science/article/pii/S0263822319306087.

Ziemke, P., Frenzel, T., Wegener, M., Gumbsch, P., 2019. Tailoring the characteristic length scale of 3D chiral mechanical metamaterials. Extreme Mech. Lett. 32, 100553. http://dx.doi.org/10.1016/j.eml.2019.100553, URL https://www.sciencedirect.com/science/article/pii/S2352431619302214.